Late Pleistocene-Holocene slip rate along the Hasi Shan restraining bend of the Haiyuan fault: implication for faulting dynamics of a complex fault system

R. Matrau, Y. Klinger, J. van Der Woerd, J. Liu-zeng, Z. Li, X. Xu, R. Zheng

AGU100 ADVANCING EARTH AND SPACE SCIENCE

Tectonics

RESEARCH ARTICLE
10.1029/2019TC005488

Key Points:
- Slip rate along the Hasi Shan section of the Haiyuan fault is determined from numerous offsets and cosmogenic exposure dates over a period of 50,000 years
- The Hasi Shan fault strand horizontal slip rate is about 3.2 mm/year; this rate is stable over 50,000 years; the uplift rate is about 0.5 mm/year
- Combining slip rate for the Hasi Shan strand and all subparallel stands yields a slip rate of 5 to 7 mm/year for the Haiyuan fault system

Supporting Information:
- Supporting Information S1

Correspondence to:
Y. Klinger,
klinger@ipgp.fr

Citation:
Matrau, R., Klinger, Y., Van der Woerd, J., Liu-Zeng, J., Li, Z., Xu, X., & Zheng, R. (2019). Late Pleistocene-Holocene Slip Rate Along the Hasi Shan Restraining Bend of the Haiyuan Fault: Implication for Faulting Dynamics of a Complex Fault System. *Tectonics*, *38*, 4127–4154. https://doi.org/10.1029/2019TC005488

Received 8 JAN 2019
Accepted 21 SEP 2019
Accepted article online 19 OCT 2019
Published online 4 DEC 2019

Late Pleistocene-Holocene Slip Rate Along the Hasi Shan Restraining Bend of the Haiyuan Fault: Implication for Faulting Dynamics of a Complex Fault System

R. Matrau[1,2], Y. Klinger[1], J. Van der Woerd[3], J. Liu-Zeng[4], Z. Li[4], X. Xu[5], and R. Zheng[4]

[1]Université de Paris, Institut de physique du globe de Paris, CNRS, Paris, France, [2]Physical Science and Engineering, Now at King Abdullah University of Science and Technology, Thuwal, Saudi Arabia, [3]Institut de Physique du Globe de Strasbourg, UMR 7516 CNRS Université de Strasbourg, Strasbourg, France, [4]State Key Laboratory of Earthquake Dynamics, Institute of Geology, China Earthquake Administration, Beijing, China, [5]Institute of crustal dynamics, China Earthquake Administration, Beijing, China

Abstract The Haiyuan fault is a major left-lateral strike-slip fault at the boundary between northeast Tibet and the Gobi platform. Combining measurements of offset alluvial terraces with ^{10}Be-^{26}Al cosmogenic radionuclides dating, we bracket the late Quaternary slip rate along the Hasi Shan fault section (37°00′N, 104°25′E) of the Haiyuan fault. At our reference site, terrace-riser offsets for five successive terraces range from ~5 to ~200 m, and associated cosmogenic radionuclide ages range from 9 ± 3 to 44 ± 7 kyr. These measurements yield a geological slip rate between 2.7 and 3.0 mm/year. Extending the offset measurements to the entire Hasi Shan front, it yields a slip rate of 3.2 ± 0.2 mm/year over the last ~50 kyr. Our rate is consistent with the lower estimates of other long-term rates of 4 to 5 mm/year, as well as with geodetic rates of 3 to 5 mm/year, determined in the same area. About 150 km farther west, however, Holocene terraces and moraines offsets have suggested higher slip rate values, between 6 and 15 mm/year. We interpret such discrepancy between rates determined along the western section of the Haiyuan fault and rates determined in the Hasi Shan section as being related to the complex geometry of the Haiyuan fault system along its eastern part, with several active strands moving at the same time and resulting in distributed slip among several sections of the fault system.

1. Introduction

The Haiyuan fault, together with the Altyn Tagh fault, defines the northern boundary of the Tibetan blocks. These two faults form a 3,000-km-long left-lateral strike-slip fault system that enables eastward extrusion of Tibet relative to Eurasia, in response to the Indo-Asia collision (Figure 1; Tapponnier & Molnar, 1977). Although the length and clear morphology of these faults make it the largest active strike-slip fault system of Asia, more quantitative constraints are needed to understand how deformation is accommodated along its different sections. The Haiyuan fault crosses the Chinese provinces of Qinghai, Gansu, Ningxia, and Shaanxi and separates the highly deformed northern Tibetan block to the south, from the undeformed Gobi Ala Shan platform to the north (Burchfiel et al., 1991; Deng et al., 1986; Gaudemer et al., 1995). The ~1,000-km-long left-lateral strike-slip fault runs from 98°E to 107°E, connecting shortening in the Qilian Shan at the eastern termination of the Altyn Tagh fault to the extensional tectonics of northeastern China in the Wei He graben (e.g., Meyer et al., 1998; Peltzer et al., 1985; Peltzer & Saucier, 1996). Near 102.3°E, the fault splays in two main branches, the Zhongwei fault to the north and the main Haiyuan fault strand to the south (Figure 1). The Zhongwei fault reconnects with the main Haiyuan strand about 400 km eastward, near the city of Guyuan (106°E). The main Haiyuan fault strikes approximately N100°E west of the Huang He (Yellow River) and progressively veers southward to reach N140°E east of the Huang He, and about N170°E along the Liupan Shan. Eventually, it resumes to N150°E west of the Wei He graben.

Several major earthquakes occurred along the central Haiyuan fault (Figure 1). On 16 December 1920, an earthquake of magnitude M~8 ruptured 220 km of the Haiyuan fault between the cities of Jingtai to the west, and Guyuan to the east (Deng et al., 1986; Zhang et al., 1987), with an estimated maximum coseismic displacement of ~5 m (Ren et al., 2016). It was followed 1 week later by a large aftershock of magnitude M~7. Another major earthquake of magnitude M~7.7 occurred on 23 May 1927, close to the western

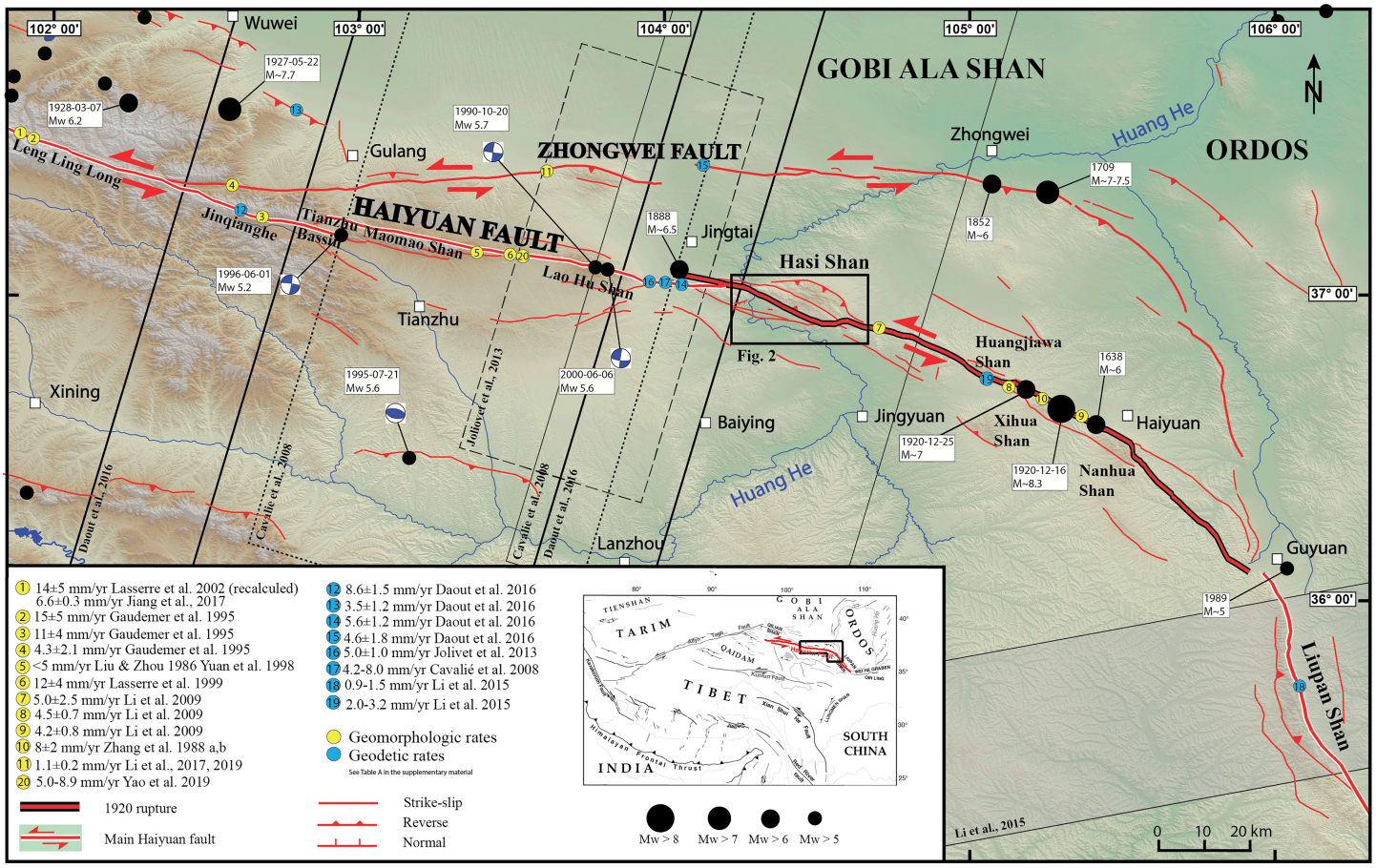

Figure 1. Active faults along Haiyuan fault system. Topography ASTER GDEM (30-m resolution; https://lpdaac.usgs.gov/). Earthquakes (black dot) and focal mechanisms from USGS. Yellow and blue circles are geomorphic and geodetic slip rates available in literature (see also Table S1), respectively. Dotted, dashed, and continuous black rectangles are InSAR swaths. Black rectangle outlines Figure 2.

Haiyuan-Zhongwei faults junction. This earthquake is believed to have ruptured a thrust-fault system north of the Haiyuan fault (Gaudemer et al., 1995; Xu et al., 2010). Along the Zhongwei fault, a major earthquake occurred in 1709, with an estimated magnitude M7–7.5 (Min et al., 2001). In addition, paleoseismological trenches along the Haiyuan fault suggest that six events of different magnitude ruptured the central Haiyuan strand in the last 3,500–3,900 years (Liu-Zeng et al., 2007). Historical medium-size earthquakes have also been documented along the 1920 rupture section (Liu−Zeng et al., 2015).

The Haiyuan fault system is formed by numerous fault strands (few tens of kilometers long) with different azimuths. Hence, the Haiyuan fault system has a complex geometry. Such complexity has major implications on the distribution of the slip across the fault system, hence on the slip rate along the different branches, and eventually on the regional seismic hazard. Here, we present a detailed morphotectonic analysis of a 20-km-long section in the Hasi Shan restraining bend along the western part of the 1920 earthquake rupture (Figure 2). We document preserved offset alluvial terraces, whose ages are constrained with cosmogenic radionuclide (CRN) dating to estimate the late Pleistocene-Holocene slip rate of the fault. We interpret this slip rate in the framework sets by other studies and discuss the regional balance and distribution of the deformation in relation with the large-scale Haiyuan fault system geometry.

2. Morphotectonic Setting of the Haiyuan Fault

2.1. Large-Scale Setting

The Haiyuan fault is generally divided in three parts. The western part is about 350 km long, from 98°E to 102°E, with an average azimuth of N100, getting closer to N125 along the Leng Long Ling restraining

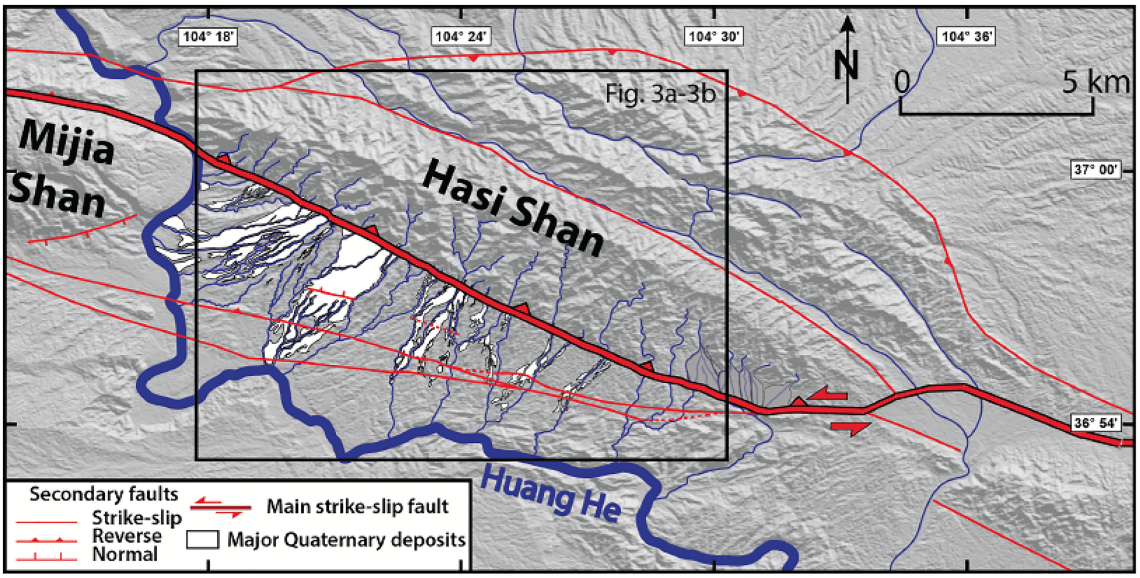

Figure 2. Tectonic setting of Hasi Shan, based on ASTER GDEM. Dissected fan surfaces of southwest Hasi Shan bajada shown in white. Black rectangle is Figure 3.

bend. The central part is ~450 km long, from 102°E to 106°E, with an azimuth between N100 and N125, depending on the sections. The eastern part is shorter, 210 km, from 106°E to 107.5°E. Its azimuth ranges between N140° and N170°.

In the following, we will mostly focus on the central part of the Haiyuan fault (Figure 1).

The main central Haiyuan strand may be divided into two parts: The first part, between longitude 101.6°E and 104.3°E, is 250 km long. It is located between the 1920 and the 1927 earthquake ruptures and is often referred to as the "Tianzhu seismic gap" (Gaudemer et al., 1995). The second part of the central segment extends for 220 km between the cities of Jingtai and Guyuan. It corresponds to the section that ruptured during the 1920 earthquake. Along that segment, east of the Mijia Shan, the fault veers toward the south, reaching N120°E along the Hasi Shan (Figure 2). After several left-stepping jogs and successive segments along the Huangjiawa Shan and Nanhua Shan, the fault eventually reaches an almost north-south direction along the ~200-km-long Liupan Shan section, which corresponds to the eastern part of the Haiyuan fault (Figure 1). This change in the fault strike around longitude 105°E results in a significant part of the deformation to become compressional, and this part is dominated by thrust motion.

Similarly, the Zhongwei fault strand, also called the Tianjing Shan fault, may also be divided into three parts according to strike. For about 160 km, from its western junction with the Haiyuan fault at 102°5 to 104°E, the western part of the Zhongwei fault strikes east-west to N85°E. The next part strikes east-west to 105°E and then veers southward until 105.8°E for a length of 190 km. This part comprises the segment that ruptured during the historical earthquake of 1709 (M7–7.5). The last part strikes N120 to north-south for 100 km and connects with the main Haiyuan fault near Guyuan.

The central part of the Haiyuan fault has been the focus of several studies aiming at determining its slip rate along different sections (Figure 1 and Table S1 in the supporting information). Most of these studies analyze only one or two offset markers. Along the Leng Long Ling section, based on high-resolution topography and offset measurements, although with poor age constraints, a slip rate of 6.6 ± 0.3 mm/year has been proposed for the Holocene period (Jiang et al., 2017). In contrast, at a nearby site, Lasserre et al. (2002) have estimated a Late Pleistocene slip rate from a 200 ± 40 m moraine offset. This rate ranges from a minimum of 11±3 mm/year with a proposed maximum Late Glacial Maximum (LGM) age (18 ± 1 kyr) for the moraine to a maximum of 15 ± 3 mm/year with ^{10}Be exposure ages of Younger Dryas boulders (13 ± 1 kyr; after updating the original cosmogenic isotope data following current calculation standards, in particular revision of the ^{10}Be production rate, e.g., Borchers et al., 2016). Although not substantiated by direct dating, Gaudemer et al. (1995) have proposed that east of the Haiyuan-Zhongwei junction, the slip rate decreases to 11 ± 4 mm/year. Farther east, along the Maomao Shan (103°E), Lasserre et al. (1999) have proposed a

slip rate of 12 ± 4 mm/year. East of the Hasi Shan, Zhang et al. (1988) have proposed a slip rate of 8 ± 2 mm/year, based on offset stream channels and radiocarbon dating. A more recent study, based on offset terraces and radiocarbon ages, has proposed a Quaternary slip rate ranging from 4 to 5 mm/year for similar areas, east of the Hasi Shan and west of the city of Haiyuan (Li et al., 2009).

Along the Zhongwei fault, values of slip rates are also contrasted. A combination of geomorphological measurements with assumption on ages, based on regional climatic variations, led Gaudemer et al. (1995) to propose a Quaternary slip rate of 4.3 ± 2 mm/year, just east of the Haiyuan-Zhongwei junction. Further east, near the city of Xishaomen (103.4°E), OSL dating of offset landforms yield slip rates ranging from 1.1 ± 0.2 mm/year (Li et al., 2017, 2019) to 4–5 mm/year (Min et al., 2001).

Short-term slip rates across the Haiyuan fault, both across the main strand and across the Zhongwei strand, based on space geodesy, are rather consistent with the slower geologic rates. Across the main strand south of the city of Jingtai, InSAR data studies yield a slip rate of about 5 ± 1 mm/year (Cavalié et al., 2008; Daout et al., 2016; Jolivet et al., 2012). Similarly, GPS measurements yield a slip rate of 3 to 5 mm/year (Gan et al., 2007; Zheng et al., 2013). Across the Zhongwei strand, InSAR yields a slip rate of 3.7 ± 1.3 mm/year (Daout et al., 2016).

2.2. Hasi Shan Setting

Our study focuses on the 20-km-long section (from 104.33°E to 104.55°E) of the Haiyuan fault located at the southern front of the Hasi Shan (Figures 1–3). West of the Hasi Shan, the main fault strikes N105°E. When it reaches to the Hasi Shan, where the fault crosses the Huang He, it veers southward to strike N120°E along the southern front of the Hasi Shan. Further east, it bends back northward through left-stepping pull-apart basins to reach N112°E east of the Hasi Shan. Hence, these changes in fault strike imply a localized compressional zone resulting in uplifted topography up to 3,000 m asl. Indeed, the Hasi Shan forms a restraining bend.

The Hasi Shan is a set of two subparallel ranges, 35 km long and 15 km wide, (Figure 2). Each of these ranges is bounded on either side by faults, likely to be partly reverse, forming a positive flower structure typical of a transpressional system. Evidence for strike-slip faulting is clear along the main active fault that ruptured in 1920 along the southern front, and much less along the other faults, although cumulative left-lateral offsets can be mapped along parts of the other faults (Figure 2; e.g., Tapponnier & Molnar, 1977; Deng et al., 1984; Burchfiel et al., 1991; Gaudemer et al., 1995; Su et al., 2019).

Additional faults cutting through the frontal alluvial fans can also be seen south of the main active fault associated to the trace of the Tertiary Haiyuan fault zone (Gaudemer et al., 1995; Gansu geological Bureau, 1975, Geological map of Gansu province, 1:10,000,000, Geological press, Beijing). These faults affect the Late Quaternary sediments (Figure 3), attesting of recent activity, although cumulative offsets remain small and suggest that these faults accommodate only limited deformation.

Here, we focus our study on the southern main frontal fault bounding the Hasi Shan (Figure 3). The main fault shows clear evidence of cumulative motion, in addition to the 1920 earthquake displacement still visible as left-laterally offset alluvial fans and streambeds. In many places, evidence of vertical displacement can also be found, as cumulative scarps across terraces, or in sections where the main Haiyuan fault is a north dipping thrust with oblique slip.

The main active fault separates the uplifted Paleozoic bedrock (Silurian metasedimentary schists and Devonian coarse conglomerates) forming the core of Hasi Shan, to the north, from folded orange-yellow-colored Neogene sandstones and conglomerates covered unconformably by white-gray Quaternary alluvial fans that form the apron of the mountain range (Figure 3a; Gansu geological Bureau, 1975, Geological map of Gansu province, 1:10,000,000, Geological press, Beijing). These alluvial fans originate from the erosion products of the Hasi Shan that are directly deposited at the outlet of the local small catchments, which are on average 1.5 to 3 km in width and 3 to 4 km in length (Figures 2 and 3).

Because the range front is steep, the local rivers draining the Hasi Shan are deeply incised, and outlets are most often characterized by narrow riverbeds with no, or limited, alluvial deposition upstream from the outlet. South of the range front, however, alluvial fans and terraces develop in a highly dissected bajada, which pattern could be partly controlled by the underlying Neogene bedrock, resulting in numerous places in long

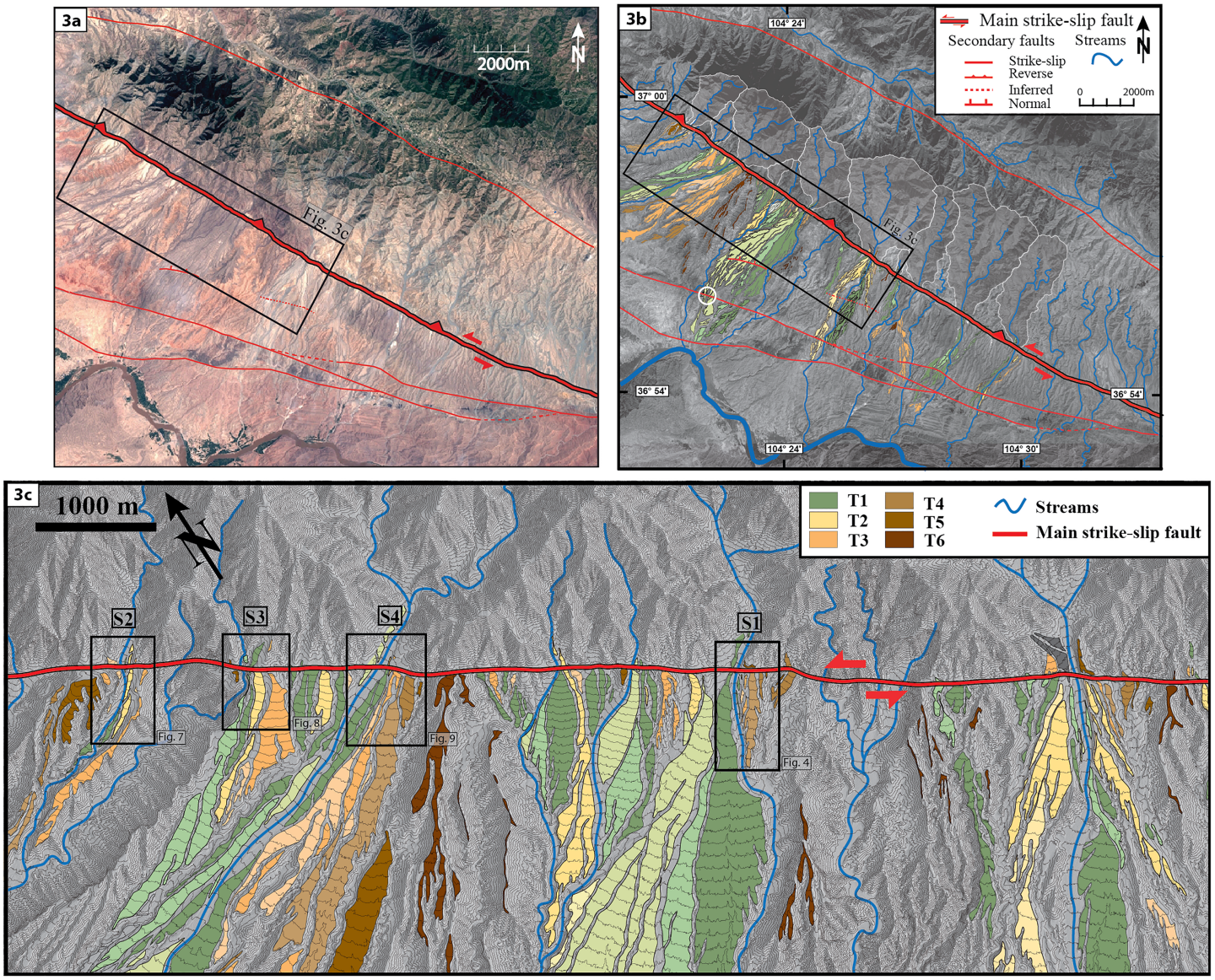

Figure 3. (a) Multispectral Pleiades satellite image of studied fault segment. (b) Morphotectonic map of Hasi Shan fault segment based on panchromatic Pleiades image (0.5-m resolution). Catchment areas are outlined in white. Colored patches are alluvial and fan surfaces. White circle shows location of offset along secondary fault. Black rectangle is location of Figure 3c. (c) Enlarged morphotectonic map based on high-resolution DEM computed from tristereo Pleiades images. Contour lines every 10 m. Black rectangles are location of Sites S1, S2, S3, and S4 and Figures 4, 7, 8, and 9, respectively.

narrow strips of alluvial terraces connecting to the local base level formed by the Huang He. Incision is strongly controlled by the size of the catchments of the individual streams, small catchments with less bedload will incise much deeper forming narrow valleys, and larger catchments with more sediments will incise less and abandon successions of terrace levels (e.g., Van der Woerd et al., 2001). Overall, the best-preserved fans are located on the western part of the Hasi Shan southern front, whereas the eastern piedmont is more degraded, consisting mainly of incised alluvial deposits and bedrock with few fan remnants (Figures 2 and 3).

3. Methodology

3.1. Image Processing and Offset Measurements

To document the morphology of the Hasi Shan front, we used high-resolution tristereo Pleiades images (0.5-m resolution). The images have a span of 20 km × 17 km, covering the entire southern front of the

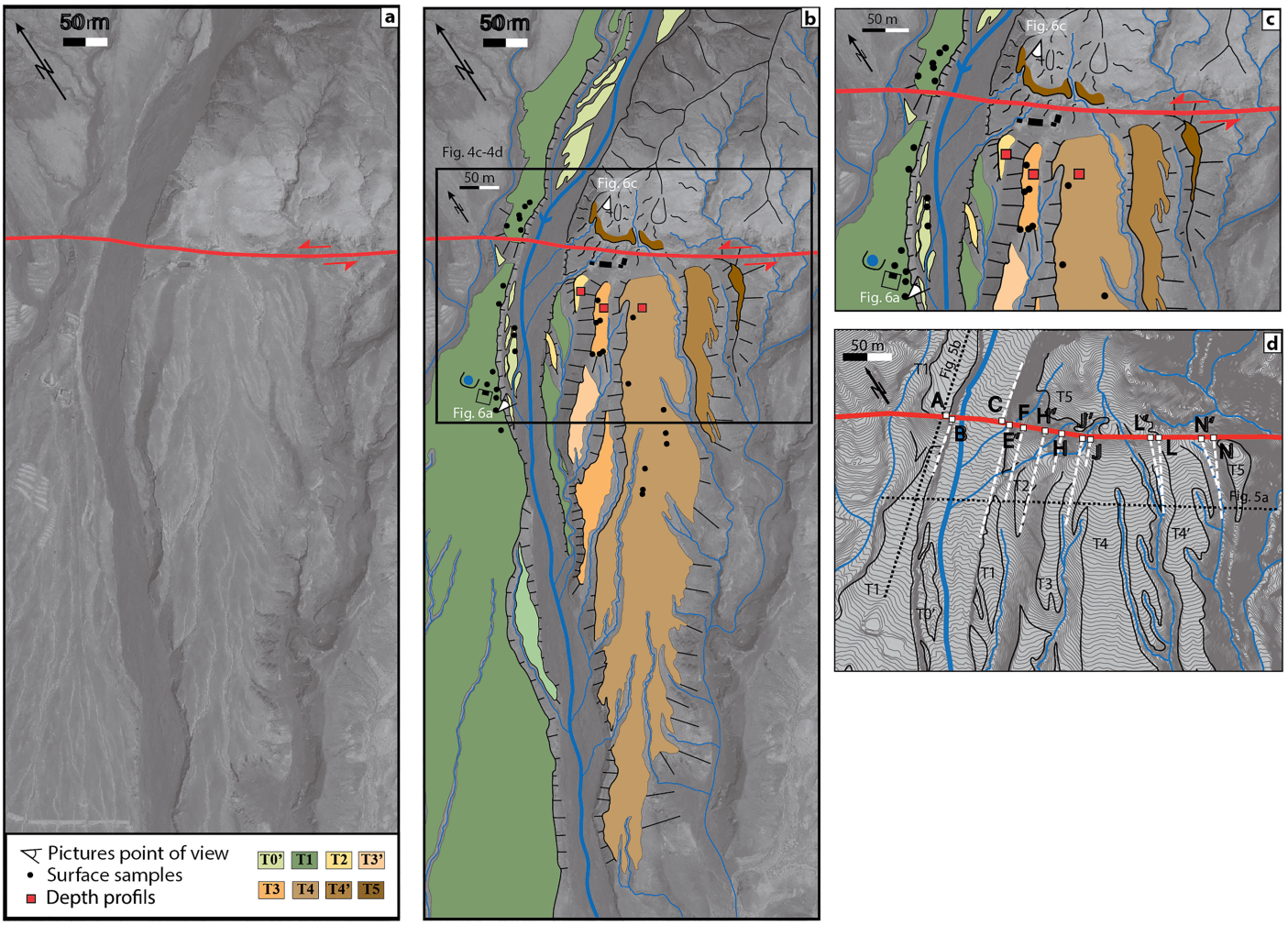

Figure 4. (a) Enlargement of Pleiades image of Site S1. (b) Geomorphic interpretation. Black frame outlines location of Figures 4c and 4d. (c) Detailed mapping. Red squares and black dots locate, respectively, depth-profile and surface samples. (d) Topography from LiDAR DEM. Dashed white lines indicate piercing lines for offset measurements. White squares with letter labels are piercing points, summarized in Table 1. Dashed black lines are topographic profiles in Figures 5a and 5b.

Hasi Shan. We computed a high-resolution digital elevation model (DEM; resolution of 0.5 m per pixel, down-sampled to 2 m) using image correlation techniques and the free software package MicMac (Rosu et al., 2015). The Pleiades images and the associated DEM were locally complemented by airborne Lidar data (Liu et al., 2013) centered on a chosen reference site (Figures 4a–4d). These data allow constructing a local DEM with a centimeter ground resolution. These different data sets were used to map in details alluvial fans along the 20-km-long Hasi Shan fault section. Most of these fans are characterized by several levels of inset terraces (Figures 3a, 3b, and 3c), which formed in response to the combined effect of incision and deposition, and fault activity (e.g., Bull, 1991; Lasserre et al., 1999; Li et al., 2005; Sieh & Jahns, 1984; Van Der Woerd et al., 2002; Weldon, 1986). Specifically, inset terraces are characterized by flat surfaces limited by risers separating successive terrace emplacements.

We chose a reference site S1 (Figure 3c) where the terrace morphology is nicely developed and where the river outlet is sharply defined. At Site S1 we mapped the inset terraces using the high-resolution Lidar DEM and systematically measured offsets of the downstream terraces relative to the river outlet. Then, each terrace level has been dated (see next sections). Assuming similar climatic and tectonic processes along the entire Hasi Shan section, we used the sequence of terraces and risers identified at Site S1 as a template to identify similar terrace sequences at three other catchments along the Hasi Shan.

Geomorphic offsets are measured by matching the risers of the same terrace on both sides of the fault. A terrace riser piercing point is defined as the intersection between the terrace riser and the mapped fault trace. However, risers are not always continuous to the fault trace due to postdepositional erosion or width of the fault zone. In addition, especially downstream from the fault, the river channel becomes wider, and the riser is often not vertical. Thus, realigning the top or the base of the riser with its counterpart across the fault leads to differences (Figure S1) that are factored into the uncertainty attached to each measurement. Eventually, we define our preferred offset value as the projection of the best-preserved part of the riser into the fault trace. When the terrace is not preserved upstream, as it is the case for most of the terraces at Site S1, instead, we used the riser carved in the bedrock as an upstream piercing line. Because imagery and topography are at high resolution, the main source of uncertainties in offset measurements comes from the identification of the different piercing points. Indeed, patterns related to fault scarp, riser geometry, and local erosion of terraces are considered when accounting for uncertainties (e.g, Gaudemer et al., 1995; Gold et al., 2009; Meriaux et al., 2012).

3.2. CRN Dating and Age Determination

CRN dating is nowadays commonly used to infer the ages of alluvial terraces from surface and subsurface samples in a wide range of tectonic and climatic contexts (e.g., Anderson et al., 1996; Balco et al., 2008; Delmas et al., 2018; Gold et al., 2015; Gosse & Phillips, 2001; Guilbaud et al., 2017; Hancock et al., 1999; Hetzel, 2013; Lal, 1991; Le Béon et al., 2010, 2012; Meriaux et al., 2004; Perrineau et al., 2011; Repka et al., 1997; Saint-Carlier et al., 2016; Van der Woerd et al., 1998, 2006; Yang et al., 2018; Yang et al., 2019). At Site S1, we collected quartz-rich pebbles and cobbles from the terrace surfaces and amalgamated quartz-rich gravel samples along depth profiles in 2- to 3-m-deep pits dug within the terraces to measure the concentration of ^{10}Be and ^{26}Al. The concentration N for the radionuclide n can be calculated as a function of depth z (cm), time t (year), and erosion rate ε (cm/year) as written in equation (1) (e.g., Braucher et al., 2003; Gosse & Phillips, 2001; Lal, 1991):

$$N_n(z,t,\varepsilon) = N_{0,n}e^{-\lambda_n t} + \sum_i \left(\frac{P_{i,n}}{\mu_i \varepsilon + \lambda_n} e^{-(\mu_i z)} \cdot \left[1 - e^{-(\mu_i \varepsilon + \lambda_n)t} \right] \right), \quad (1)$$

where i represents the different production pathways (neutron and muons), $P_{i,n}$ is the surface production rate at the sampling location for the radionuclide n via the production pathway i (in at·g^{-1}·year^{-1}), λ_n is the decay constant for the radionuclide n (in year^{-1}), and μ_i the absorption coefficient defined as the ratio of the density ρ (in g/cm^3) over the attenuation length of the production pathway i Λ_i (in g/cm^2).

Samples were analyzed following the standard chemical processing from Kohl and Nishiizumi (1992). The CRN surface ages were calculated using the CRONUS-Earth calculator v3, using the time constant scaling scheme "St" (Lal, 1991; Stone, 2000) with a sea level high-latitude production rate of 4.01 ± 0.33 at·g^{-1}·year^{-1} (Borchers et al., 2016; Balco et al., 2008; https://hess.ess.washington.edu/math/v3/v3_age_in.html; Table 2). The CRN subsurface concentrations were modeled with relative contributions of 97.8%, 1.5%, and 0.65% and attenuation lengths of 160, 1,500, and 4,320 g/cm^2 for neutron, negative muons, and fast muons, respectively (Balco, 2017; Braucher et al., 2003; Marrero et al., 2016), and a density of 2.2 for the lower conglomerate and a density of 1.4 for the loess top layer (Figure 10; Table 2)

Interpretation of surface and subsurface sample concentrations and ages was done separately for both ^{10}Be and ^{26}Al nuclides. CRN concentrations were measured in surface and subsurface samples for four and three terraces, respectively (Figure 4; Table 2). Comparison between subsurface model age and surface ages distribution helped assess the degree of postdepositional surface modification (e.g., Delmas et al., 2018; Ryerson et al., 2006; Saint-Carlier et al., 2016). Indeed, classically, model exposure ages from surface samples are interpreted as representing the abandonment age of an alluvial surface, meaning when the surface is no longer permanently flooded. Nevertheless, soon after abandonment, surfaces might still be occasionally overflooded, leading either to redeposition of sediments or to partial erosion, which could alter the determination of the terrace age biasing it toward younger ages (erosion) or toward older ages (reworking of pre-exposed sediments).

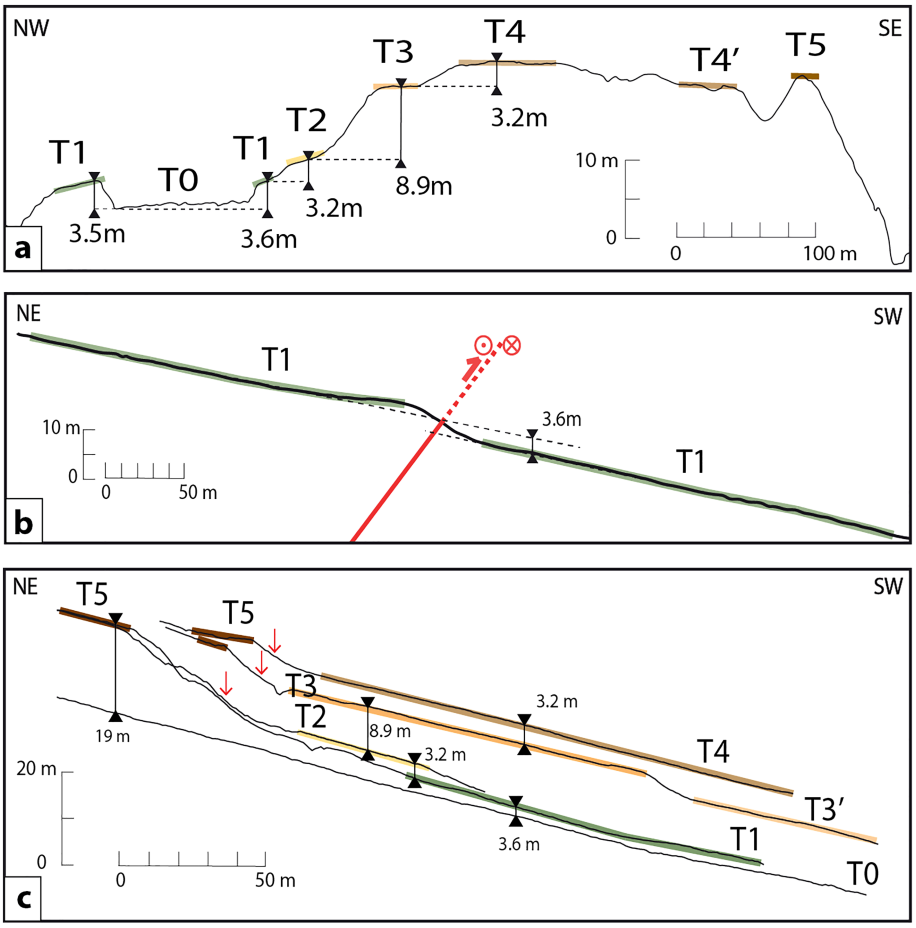

Figure 5. (a) Fault parallel topographic profile at Site S1. Color coding of terraces as in Figure 4. (b) Fault perpendicular topographic profile of T1 on right bank of active streambed. (c) Projections of fault perpendicular topographic profiles on left bank of active streambed.

4. Detailed Morphotectonic Analysis and Offsets of Inset Terraces

4.1. Site S1 Setting

Site S1 is located 36.96°N, 104.41°E, at an elevation of 1,900 m, about 600 m above the Huang He riverbed (Figure 3). At Site S1 a single 50-m-wide active streambed drains a 5-km^2 catchment and has deposited a fan complex, which is about 400 m wide near its apex, where it is cut by the fault (Figure 4). The most recent terrace (T1) is the only one that can be found both upstream and downstream from the river outlet, along the right (west) bank of the river. This terrace stretches for 7 km down to the Huang He (Figure 3b). The upstream left (east) bank of the stream is instead characterized by a steep bedrock riser. Downstream and on the left bank a swath of inset alluvial terraces covers an area about 1,000 m long and 300 m wide (Figure 4). Hence, along the left bank we documented five main levels of terraces labeled T1 to T5, with T5 being the oldest. Several additional terrace sublevels can also be recognized. T0 corresponds to the active streambed (Figure 4).

The terrace surfaces are narrow, ranging from 15 to 120 m in width. The different terrace surfaces are separated by 3- to 9-m-high risers (Figure 5a). T1 is directly standing 3 to 4 m above the main streambed, and the height of the riser T1/T0 is fairly constant downstream. T2 is preserved only in the form of two narrow patches, about 3 m above T1 (Figure 4c). Close to the river, one patch of T2 appears as a small remnant islet surrounded by T1 (Figure 6). Close to the fault trace, a piece of T2 is resting at the base of the riser T3/T2 (Figures 5 and 6). The riser T3/T2 is about 9 m high; it is the highest riser at Site S1. Metric boulders are outcropping in the slope of the riser T3/T2 (Figure 6). T3 is subdivided in two surfaces, separated by a sublevel

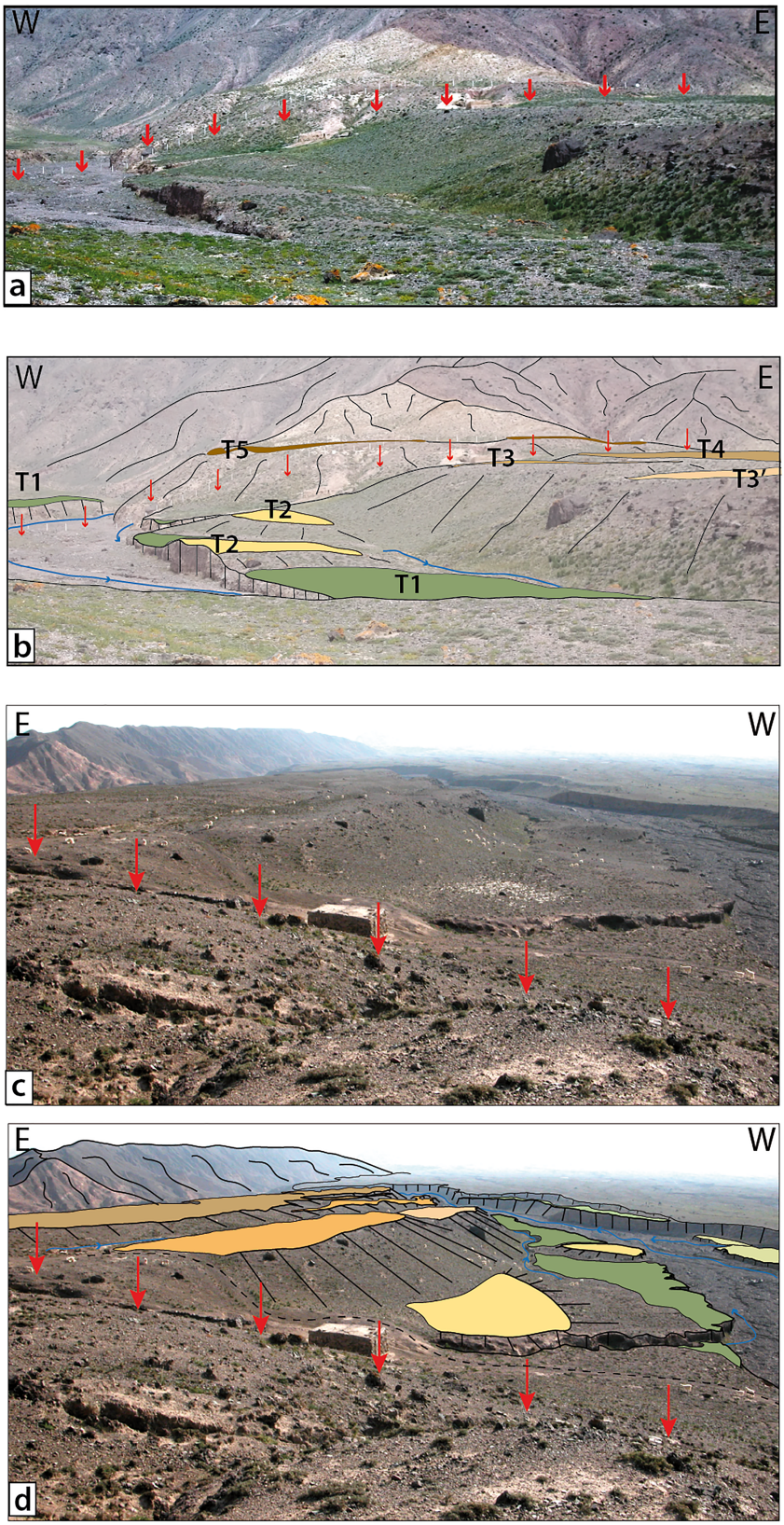

Figure 6. (a) NE looking view of inset terraces at Site S1. (b) Interpretation of picture in Figure 6a. Red arrows outline fault trace. (c) SW looking view at Site S1. (d) Interpretation of picture in Figure 6c. Edge of house in foreground is about 5 m long.

T3′ located 4 to 5 m below T3 (Figures 4 and 5). The best-preserved 120-m-wide terrace T4 on the left bank of the stream is separated from T3 by a 3-m-high gently sloping riser (Figure 5). East of T4 two additional terraces, T4′ and T5, are separated by risers of 3 and 5 m, respectively. Although these terraces are stratigraphically older than T4, they stand lower in elevation due to the convex shape of fan surfaces (Figure 5a). An even higher terrace level is also mapped as terrace T6, which remains only on narrow crests. It is not preserved near the fault at Site S1 but about 1 km downstream and stands about 80 m above T1 (Figure 3).

Upstream of the fault, along the left bank, we mapped a terrace remnant about 18 to 20 m above the active streambed (Figure 4). This surface corresponds to a strath terrace, which bedrock embankment can be seen in the riverbed. It is standing high above the active stream, and higher than any downstream surface; we thus tentatively correlate it with T5, which is the oldest surface downstream (Figure 5c).

Along the right bank, Terrace T1 is the only terrace that is preserved, and it can be traced across the fault zone (Figure 4). Where the fault cuts through T1, a 4-m-high southwest facing scarp (Figure 5b) clearly indicates that this section of the fault has a vertical component, including during the 1920 earthquake, in addition to strike slip.

At Site S1, all terrace surfaces have similar compositions: They are paved with a mix of gravels, pebbles, and cobbles embedded in a consolidated silty matrix, with very limited vegetation on top (Figures 4 and 6). No significant loess cover can be found on any of these terraces. Overall, the terraces are planar, sloping southwestward, and are only affected by regressive channel erosion. Recent anthropic modification of the surfaces is limited (Figure 4).

4.2. Offsets at Site S1

As described above, only terrace T1 on the right bank can be traced across the fault at Site S1. Using satellite imagery and topographic data, we could measure an individual horizontal offset of 5.8 ± 0.5 m for the riser T1/T0 (Figure 4d). It is the smallest offset measured at this site, and it must thus correspond to the coseismic offset of the 1920 rupture (M~8.3). This offset measurement is in agreement with a coseismic slip of 4 ± 2 m inferred for the 1920 earthquake rupture along the Hasi Shan segment by Ren et al. (2016), using field measurements and LiDAR data, suggesting that no significant erosion occurred since 1920 at that site.

Along the left bank of the stream, no terrace deposits are preserved upstream of the fault, whereas all the offset risers are located along the downstream left bank of the stream. Therefore, we used the eastern side of the upstream channel located at the base of the bedrock riser of T5 as the position of the various risers at time of formation. We assume that this rocky riser has not been significantly eroded during the time spanning the emplacement of the inset terraces. Indeed, we cannot exclude that at the time of their emplacement, each terrace would have had a matching part upstream that was later eroded. Hence, all cumulative offsets measured relative to this piercing point upstream have to be considered as minimum offsets (e.g., Meriaux et al., 2012). Downstream, all terrace risers have a curved shape. Terraces T2, T3, and T4 curve eastward toward the fault trace, whereas terraces T4′ and T5 curve westward. Although these different patterns might result from meandering, we cannot rule out that they might result instead from postdeposition modification, and it has to be considered during the offset measurements (Cowgill, 2007).

Similarly to T1/T0 along the right bank, the offset of T1/T0 along the left bank is 5.4 ± 0.5 m, pointing to an individual coseismic event offset as well. This is the smallest offset measured at Site S1. As the southern bench of T2 appears to be an isolated remnant of the surface, surrounded by T1, we used instead the northern strip of T2 located at the foot of T3/T2 riser nearby the fault trace to define the T2 piercing line. T2 is the smallest terrace remnant at Site S1 and its lower riser T2/T1 presents a smooth and low-angle slope difficult to detect on satellite images. However, T2/T1 is well defined on the DEM (Figure 4d) and on topographic profiles (Figure 5a). The terrace seems to become narrower southward, suggesting that this riser might have been partly eroded away. This geometry of the riser induces uncertainties on the offset measurements. Our best reconstruction yields an offset of 15.5 +7/−3 m. Riser T3/T2 is fairly straight and parallel to the present streambed, except close to the fault where the riser veers to the east. If we assume local erosion or human activity to explain the riser veering toward east, projecting the well-defined straight riser onto the fault trace yields an offset of 34 ± 2 m. If the riser's shape is depositional, then a larger offset value of 47 ± 5 m for riser T3/T2 is estimated. Similarly, the riser T4/T3 curves eastward near the fault, inducing uncertainties on the offset measurements. Considering the projection of the straight part of the riser far from the fault towards the

Table 1
Terrace Riser Offsets (in m) at Sites S1, S2, S3, and S4

	Site 1 Offset m	Err + m	Err − m	Site 2 Offset m	Err + m	Err − m	Site 3 Offset m	Err + m	Err − m	Site 4 Offset m	Err + m	Err − m	Age ka	1 s ka
T1/T0	5.8 (AB)	0,5	0,5	5.8 (AB)	0,5	0,5	17 (D'E')	2	2	—	—	—	—	—
	5.4 (CE')	0,5	0,5	—	—	—	27 (BC)	2	2	—	—	—	—	—
T2/T1	15.5 (CF)	7	3	16 (CD)	2	2	34 (DE)	10	2	25 (AD)	2	2	9,05	2,95
T3/T2	34 (CH')	2	2	35 (EF)	2	2	51 (GH')	8	8	49 (BF)	2	2	15	2,3
	47 (CH)	5	5	44 (EF')	3	3	—	—	—	—	—	—		
T4/T3	72 (CJ')	2	2	—	—	—	—	—	—	129 (BH)	10	10	36	5,7
	78 (CJ)	2	2	—	—	—	—	—	—	—	—	—		
T4′/T4	149 (CL')	4	4	—	—	—	—	—	—	160 (BJ)	10	10	44,3	5,8
	160 (CL)	4	4	—	—	—	—	—	—	179 (BJ')	10	10		
T5/T4	198 (CN')	4	4	—	—	—	—	—	—	288 (BL)	20	20	—	—
	212 (CN)	4	4	—	—	—	—	—	—	—	—	—	—	—
T6	600	50	50	~650	—	—	—	—	—	600	20	20	—	—

Note. Letters refer to piercing points in Figures 4, 7, 8, and 9, and the uncertainties associated to the piercing points. For most risers, the upper and lower bounds of the offset are based on the shape of the riser.

fault trace, it yields an offset of 72 ± 2 m. Considering the closest point of the curved riser near the fault trace as piercing point instead, it yields an offset of 78 ± 2 m. Riser T4′/T4 does not reach the fault trace and veers westward. Our best reconstruction for T4′/T4 yields 153 ± 4 m. Similarly, riser T5/T4′ veers toward west and yields and offset of 198 ± 4 m. Although T6 is not reaching the fault trace, the projection of its position yields a loosely constrained offset of 600 ± 50 m (Table 1).

4.3. Additional Sites

In addition to Site S1, we mapped in details three other sites along the southern Hasi Shan front. These three sites were correlated with Site S1, our reference site, based on similarities in morphology. A reference marker is the 9-m-high riser T3/T2 at Site S1, which is significantly higher than the other ones at the same site. We interpret the larger height of this riser as the indication that it formed in response to some noticeable climatic fluctuation. Similarly, Terrace T6, which stands much higher than all other terraces, might also be used as a characteristic marker of a significant climatic imprint. Thus, because such climate fluctuation should affect all other catchments along the Hasi Shan as well, similarly larger risers should be found at the other sites with similarly sized catchments, which should be coeval with risers T3/T2 or T6/T5 at Site S1. In the following, we describe Sites S2, S3, and S4 (Figure 3c) that present the clearest patterns of inset terraces similar to Site S1. Table 1 summarizes the offset measurements at all sites.

Site S2 is the westernmost fan complex along the Hasi Shan section. It is located 5.5 km northwest of Site S1, at an elevation of 1,700 m. At Site S2, the narrow alluvial terraces extend for 2 km with a maximum width of 350 m near the fault trace. Along the left bank, we mapped three levels of Terraces T1, T2, and T3 (Figure **7**). Unlike Site S1, remnants of the terraces are preserved both upstream and downstream of the fault. The offset of T1 is 5.8 ± 0.5 m, consistent with a single coseismic displacement (Ren et al., 2016). The riser T2/T1 is reaching the fault trace on both sides of the fault and is offset 16 ± 2 m. However, a small rill is incised between T1 and T2, potentially eroding riser T2/T1 upstream, and therefore yielding only a minimum offset. The riser T3/T2 is quite linear, and the projection of the straightest part of the riser into the fault trace yields an offset of 44 ± 3 m. However, similarly to Site S1, the riser T3/T2 curves westward close to the fault, hence yielding a smaller offset of 35 ± 2 m. The riser T3/T2 is the highest riser at that site, about 20 m, and is interpreted as corresponding to the similar high riser at Site S1. The difference in absolute height between risers for the various fans and corresponding catchments may result from differences in the local characteristics of the drainage basins (e.g., Van der Woerd et al., 2001). Thus, only relative heights between risers at a same site are used to match the terrace pattern at each site with the terrace pattern at the reference site. Terrace T6, like at Site S1, is visible further southwest, about 1 km away from the fault trace on a narrow crest. Projecting its position on the fault trace yields a loosely constrained offset of 650 m (Figure 3).

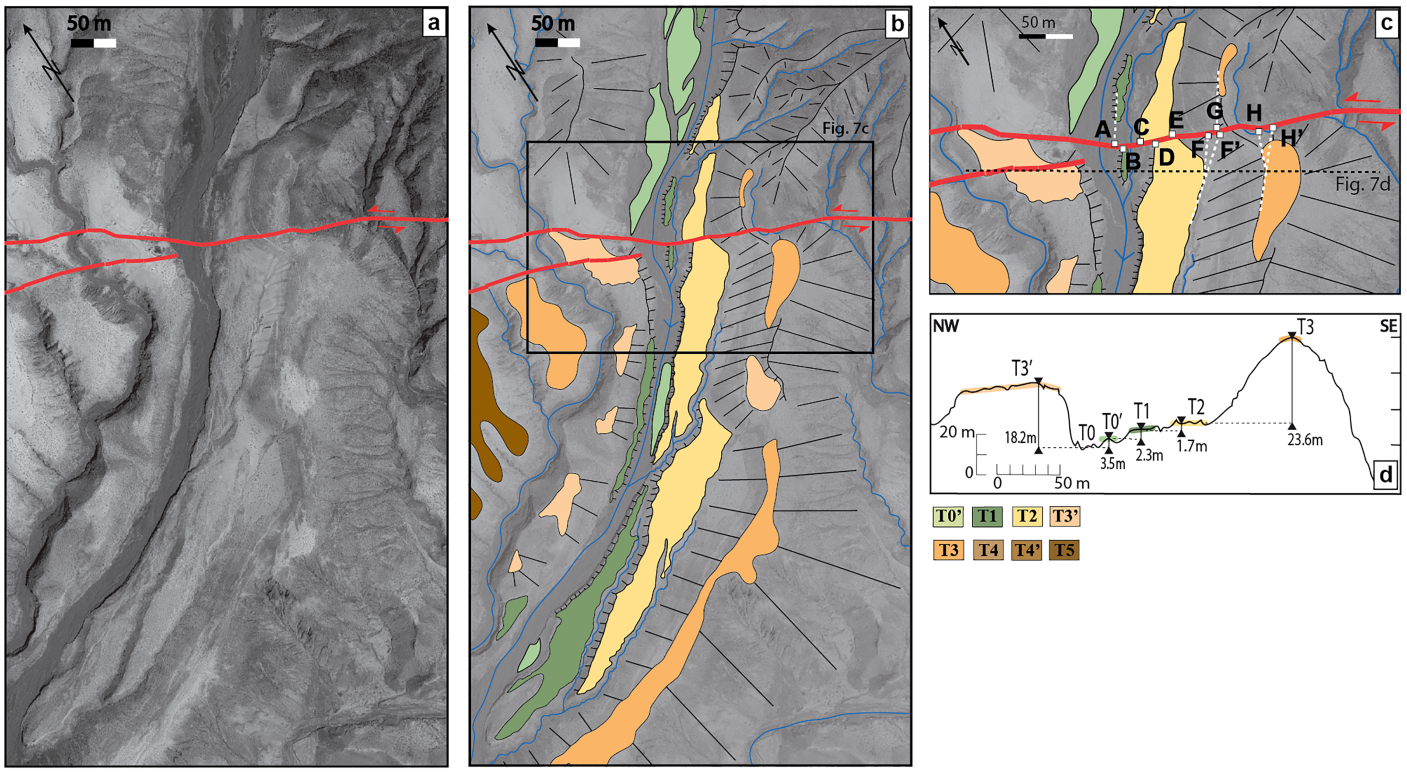

Figure 7. (a) Enlargement of Pleiades image at Site S2. (b) Geomorphic interpretation. Black frame outlines location of Figure 7c. (c) Detailed mapping. Dashed black line outlines location of topographic profile in Figure 7d. White squares with letter labels are piercing points, summarized in Table 1. (d) Fault parallel topographic profile.

Site S3 is located 4.5 km northwest of Site S1, at an elevation of about 1,850 m (Figure 3c). The 20-m-wide main active stream is narrow and incises 20–25 m in the piedmont (Figure 8). The strong incision of the active stream can be explained by the position of the catchment just east of a 180-m-deep incision, which has captured the mainstream, strongly lowering the present catchment base level as compared to the average elevation of the abandoned terraces (e.g., Van der Woerd et al., 2001; Figure 3). We mapped three main levels corresponding to Terraces T1, T2, and T3 similar to Site S1. All three levels are preserved on both sides of the fault. The geometry of Site S3, however, is more complex than the other sites because surfaces are more incised, with several streams separating remnants of terraces. The main active stream is 20 m below T1; therefore, we can assume T1 has not been flooded since its deposition. T1 is offset by 17 to 27 m. Upstream of the fault, T1 is laying directly below T3. T2 seems to have been eroded, with only a small remnant surface preserved close to the fault trace. We assume T1 upstream to be laying on top of a bulge of bedrock because the stream between T1 and T3 is deviated westward close to the fault trace due to harder material difficult to erode (Figures 8b and 8c). Our reconstruction yields a riser T2/T1 offset of 34 +10/−2 m. Upstream of the fault, T3 is a narrow surface that does not reach the fault trace. T3 downstream of the fault veers westward close to the fault trace. Our best reconstruction for riser T3/T2 yields an offset of 51 ± 8 m.

Site S4 is located 3.2 km northwest of Site 1 at an elevation of 1,870 m (Figure 3c). The terraces reach the Huang He riverbed 5 km southwest of the apex of the fan. The characteristic riser T3/T2 is very clear at Site S4, despite the fact that preserved remnants of T2 are scarce. Along the right bank, no terraces are preserved near the fault zone (Figure 9). A right step in the fault trace forms a local push up on the left bank, complicating the reconstruction of the different terraces across the fault. T1 is not preserved upstream of the fault. Therefore, we measured the offset between T2/T1 downstream of the fault and T2/T0′ upstream of the fault. It yields an offset of 25 ± 2 m. T2 and T3 are preserved both upstream and downstream of the fault, although T2 consists of two narrow stripes close to the fault. Our reconstruction yields an offset of 49 ± 2 m for riser T3/T2 offset. T4, T4′, and T5 are not preserved upstream of the fault. Similar to Site S1,

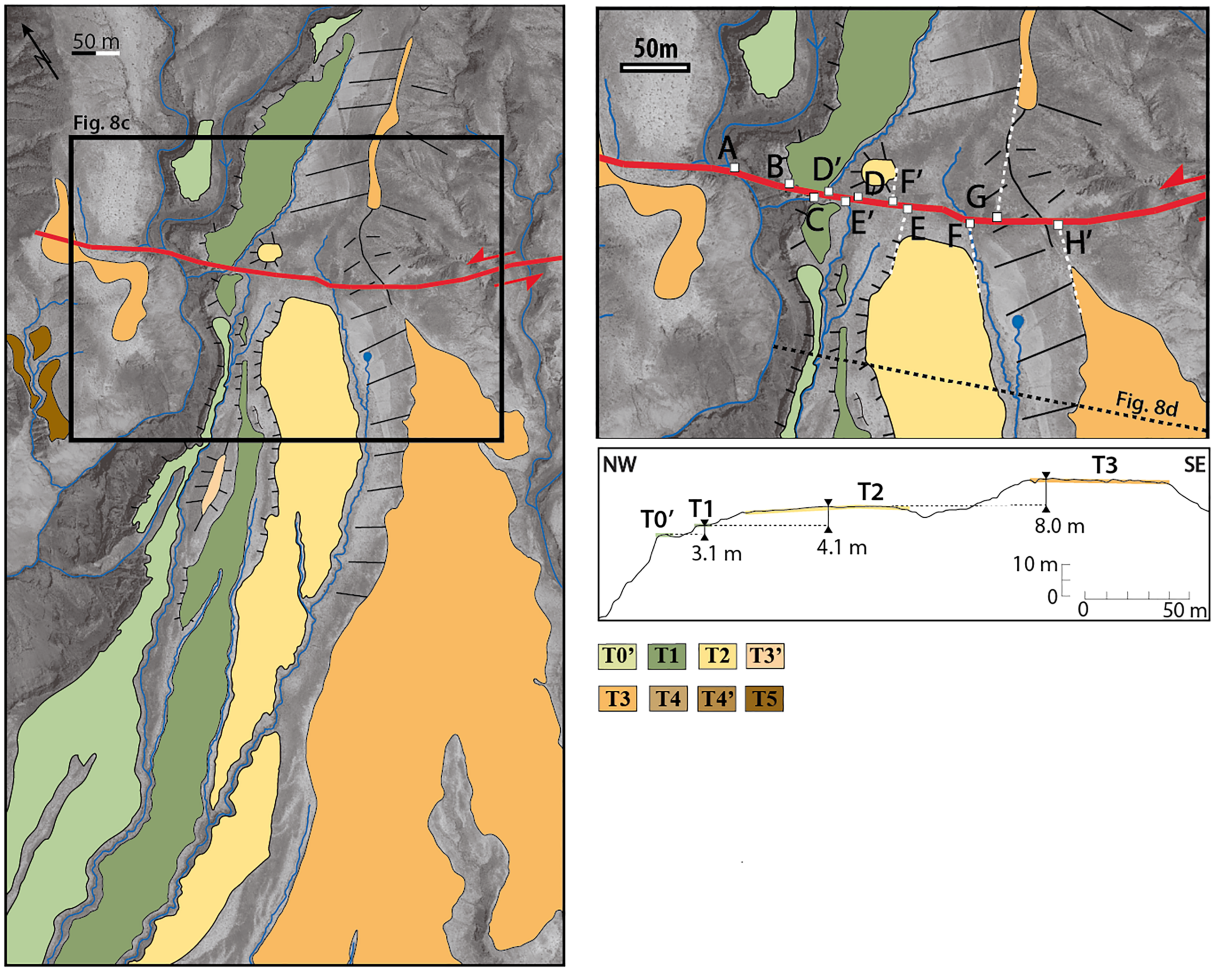

Figure 8. (a) Enlargement of Pleiades image at Site S3. (b) Geomorphic interpretation. Black frame outlines location of Figure 8c. (c) Detailed mapping. Dashed black line outlines location of topographic profile in Figure 8d. White squares with letter labels are piercing points, summarized in Table 1. (d) Fault parallel topographic profile.

we matched the risers of T4, T4′, and T5 downstream of the fault with the main preserved riser upstream of the fault (T3/T2), therefore yielding minimum offsets. We measure minimum offsets of 129 ± 10 m for T4/T3, 160 to 179 m for T4′/T4, and 288 ± 20 m for T5′/T4′. Similar to Sites S1 and S2, a large remnant of Terrace T6 limits the terraces of Site S4 to the east. Here, Rerrace T6 reaches the fault trace and defines a well-constrained offset of 600 ± 20 m (Figure 3c).

5. CRN Exposure Dating at Site S1

The well-preserved and planar inset terraces at Site S1 were targeted for sampling. Overall, erosion of the terraces is limited to regressive channels (Figure 6) that leave large patches of terrace surfaces unaffected by postdeposition modification. Hence, we can assume that erosion has limited impact, if any, on the calculated exposure ages. Similarly, although lower Terrace T2 is partly covered by a thin veneer of loess (30–40 cm), most of the terraces have no significant loess cover that would affect the exposure age determination (Figure 6).

We collected a total of 28 quartz-rich well-rooted pebbles and cobbles ranging from 2 to 10 cm in diameter on the surfaces of T1, T3, and T4 (black dots on Figure 4), and we excavated three ~2-m-deep pits in T2, T3, and T4, to collect samples for depth profiles (red squares in Figure 4). In each pit, we sampled seven to nine layers every 25 to 30 cm of amalgamated samples composed of 30 to 50 quartz-rich gravels (Figure 10).

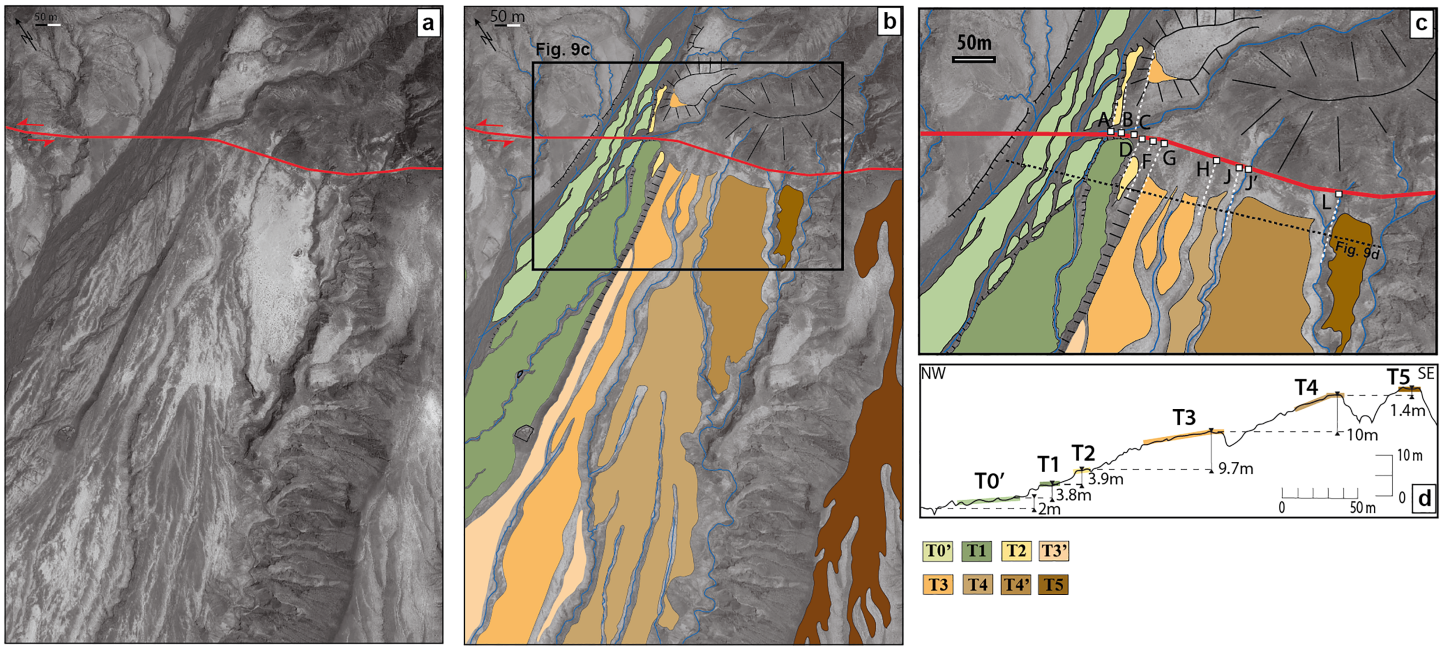

Figure 9. (a) Enlargement of Pleiades image at Site S4. (b) Geomorphic interpretation. Black frame outlines location of Figure 9c. (c) Detailed mapping. Dashed black line outlines location of topographic profile Figure 9d. White squares with letter labels are piercing points, summarized in Table 1. (d) Fault parallel topographic profile.

We analyzed both ^{10}Be and ^{26}Al for all our samples (Table 2). Overall, there is a fair agreement between ^{10}Be and ^{26}Al data, except for terrace T4 for which surface samples show lower ^{26}Al concentrations (about 20% on average; Figures 10 and 11). Two samples in the deepest part of the depth profile in T2 have significantly high ^{26}Al/^{10}Be ratios of 7.8 and 9.92 and were not considered for the age modeling. We observe an overall agreement in ^{10}Be and ^{26}Al concentrations between the surface and the subsurface samples, which favors similar exposure histories for the surface and subsurface sediments despite their type (single cobble/amalgamated gravels) and size differences (5–10 cm/less than a few cm; Figure 10). We analyze the overall agreement between ^{10}Be and ^{26}Al data as a validation of the dating method.

We modeled the ^{10}Be and ^{26}Al concentrations in the three depth profiles assuming no erosion, as the terraces show postdepositional silty loess accumulation. As the loess is thin (<40 cm), we model the depth profiles as static two-layer deposits of density 1.4 for loess and 2.2 for the underlying conglomerate (e.g., Perrineau et al., 2011; Yang et al., 2019). A global mean sea level at high latitude spallogenic production rate of 4.01 $\pm$ 0.33 at·g^{-1}·year^{-1} for ^{10}Be (Borchers et al., 2016) and a ^{26}Al/^{10}Be spallogenic production ratio of 6.61 (Braucher et al., 2011) are used to scale the local production rates. The best fit to the samples is obtained by chi-square minimization following the method described in Yang et al. (2019); see also Hidy et al., 2010; Borchers et al., 2016; Saint-Carlier et al., 2016; Delmas et al., 2018). The range of solutions obtained is a proxy for the 1-sigma confidence level based on analytical uncertainties, which represent internal uncertainties (Figure 10; Table 3). We propagated errors on these solutions corresponding to production rate (8.22%), radioactive constant (7%), and density (10%) errors to estimate external errors (Figure 10). The best models with no erosion yield ages for T2, T3, and T4 of 16 $\pm$ 2.2, 36 $\pm$ 5, and 43 $\pm$ 6 kyr and 14 $\pm$ 2, 37 $\pm$ 5, and 46 $\pm$ 6 kyr for ^{10}Be and ^{26}Al, respectively. Inheritance is relatively small and represents less than 10% of the cosmogenic isotope concentration at the surface. Because the distributions of ^{10}Be and ^{26}Al concentrations from the surface samples for terraces T3 ($n = 6$) and T4 ($n = 8$) are in the same range of the best fitting model of the subsurface concentrations for these terraces (Figure 11), we are confident that our assumption about minor surface modification is correct and that no major bias is expected from the ages of the surface samples. This observation also suggests that inheritance of the surface samples might be on the same order, also impossible to estimate quantitatively for each individual sample. The CRN model ages of the surface samples (Figure 11; Table 2) are thus calculated assuming no erosion.

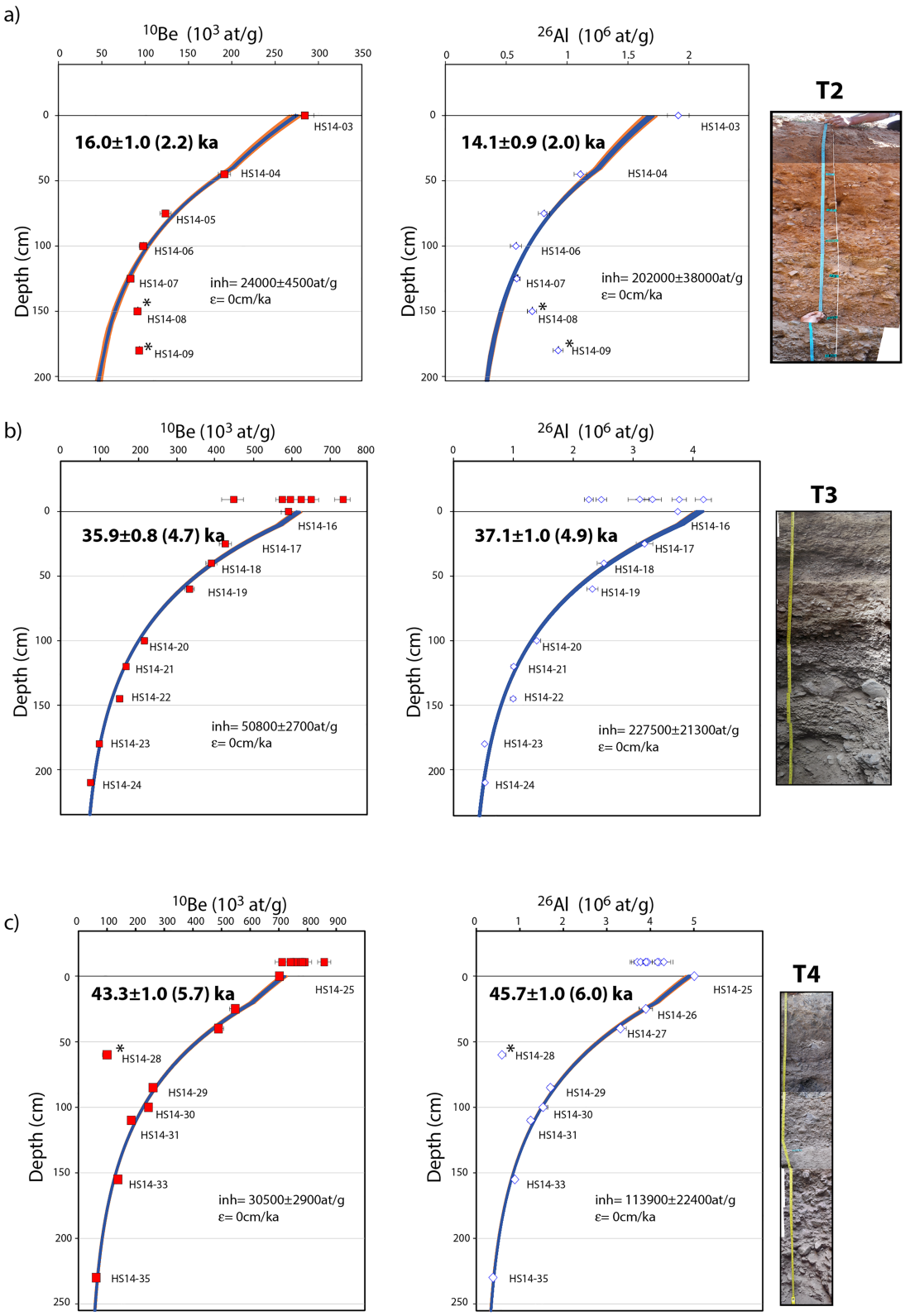

Figure 10. Cosmogenic radionuclide depth profiles derived from gravel and amalgamated samples at Site 1 for T2 (a), T3 (b), and T4 (c). Surface sample concentrations are indicated for T3 and T4. ^{10}Be to the left, ^{26}Al to the right. A global mean SLHL spallogenic production rate of 4.01 ± 0.33 at·g^{-1}·year^{-1} for ^{10}Be (Borchers et al., 2016) and a ^{26}Al/^{10}Be spallogenic production ratio of 6.61 (Braucher et al., 2011) are used to scale the local production rates and calculate ages. Model solution are indicated with internal errors (external errors within brackets).

Table 2
Analytical Results of 10Be and 26Al CRN Dating at Site S1 for 31 Surface Samples and 25 Depth Profile Samples

Sample name	Latitude (°N)	Longitude (°E)	Elevation (masl)	Depth (cm)	Loess cover (cm)	Type	Rock type	Thickness (cm)	Quartz mass (g)	9Be added (mg)	10Be/9Be	err
Terrace T0′												
YR05-22	36.96291	104.41087	1,872	0		Cobble		3	64.35179	0.36415	4.53E–13	1.39E–14
YR05-23	36.96281	104.41079	1,871	0		Cobble		4	69.52849	0.34664	2.78E–13	1.18E–14
YR05-24	36.96262	104.41068	1,868	0		Cobble		4	72.36818	0.34069	1.93E–13	5.96E–15
Terrace T1up												
YR05-02	36.96387	104.41180	1,895	0		Cobble		4	48.02127	0.35365	3.83E–13	1.15E–14
YR05-05	36.96399	104.41174	1,893	0		Cobble		3	63.47250	0.50490	5.16E–13	1.60E–14
YR05-06	36.96397	104.41183	1,894	0		Cobble		4	71.93540	0.49470	2.51E–13	7.96E–15
YR05-07	36.96399	104.41184	1,893	0		Cobble		6	63.57900	0.49850	2.35E–13	7.50E–15
YR05-08	36.96404	104.41196	1,894	0		Cobble		2	72.36340	0.50470	2.58E–13	8.42E–15
YR05-09	36.96404	104.41203	1,894	0		Cobble		3	78.52810	0.51280	6.07E–13	1.99E–14
Terrace T1down												
YR05-11-1	36.96338	104.41099	1,877	0		Cobble		8	31.20355	0.33886	2.62E–13	8.95E–15
YR05-13-1	36.96318	104.41075	1,875	0		Cobble		4	28.30883	0.30707	2.14E–13	9.41E–15
YR05-15-1	36.96247	104.41006	1,865	0		Cobble		4	27.24560	0.33620	1.50E–13	1.49E–14
YR05-16-1	36.96233	104.40983	1,862	0		Cobble		3	40.89706	0.32710	2.32E–13	7.56E–15
YR05-17-1	36.96223	104.40992	1,861	0		Cobble		3	37.69638	0.32840	1.97E–13	6.49E–15
YR05-18-1	36.96206	104.40979	1,860	0		Cobble		3	42.18071	0.32945	3.32E–13	1.05E–14
YR05-19-1	36.96189	104.40973	1,858	0		Cobble		3	39.75793	0.33488	2.75E–13	8.44E–15
YR05-21-1	36.96228	104.40999	1,864	0		Cobble		3	22.33479	0.32228	1.25E–13	4.54E–15
Terrace T2 DP												
HS14-3	36.96295	104.41202	1,880	0	0	Amalgamated gravels	qtz vein	1	19.80061	0.31299	2.69E–13	8.46E–15
HS14-4	—	—	—	45	40	Amalgamated gravels	qtz vein	1	18.58576	0.31370	1.70E–13	5.31E–15
HS14-5	—	—	—	75	40	Amalgamated gravels	qtz vein	1	15.33649	0.31340	9.05E–14	4.23E–15
HS14-6	—	—	—	100	40	Amalgamated gravels	qtz vein	1	12.62042	0.31379	5.89E–14	2.49E–15
HS14-7	—	—	—	125	40	Amalgamated gravels	qtz vein	1	41.95543	0.31321	1.67E–13	5.16E–15
HS14-8	—	—	—	150	40	Amalgamated gravels	qtz vein	1	40.19845	0.31273	1.75E–13	5.44E–15
HS14-9	—	—	—	180	40	Amalgamated gravels	qtz vein	1	40.19525	0.31260	1.79E–13	5.56E–15
Terrace T3												
YR05-34	36.96257	104.41209	1,897	0		Cobble		3	51.56130	0.32864	1.47E–12	4.44E–14
YR05-35	36.96233	104.41191	1,892	0		Cobble		5	42.33770	0.34510	1.06E–12	3.16E–14
YR05-36	36.96233	104.41185	1,889	0		Cobble		4	43.73010	0.37620	1.13E–12	3.68E–14
YR05-37	36.96203	104.41174	1,887	0		Cobble		6	53.98240	0.48980	7.39E–13	2.26E–14
YR05-38	36.96203	104.41171	1,886	0		Cobble		5	56.56490	0.51100	9.88E–13	2.96E–14
YR05-39	36.96206	104.41155	1,884	0		Cobble		4	61.83830	0.51700	1.31E–12	3.89E–14
T3 DP												
HS14-16	36.96246	104.41207	1,890	0	0	Amalgamated gravels	qtz vein	1	19.55702	0.29409	5.9184E–13	1.61E–14
HS14-17	—	—	—	25	10	Amalgamated gravels	qtz vein	1	18.34571	0.29995	3.9303E–13	1.21E–14
HS14-18	—	—	—	40	10	Amalgamated gravels	qtz vein	1	17.15632	0.29965	3.3663E–13	1.03E–14
HS14-19	—	—	—	60	10	Amalgamated gravels	qtz vein	1	17.46407	0.31185	2.8202E–13	8.62E–15
HS14-20	—	—	—	100	10	Amalgamated gravels	qtz vein	1	17.45444	0.30120	1.8941E–13	6.30E–15
HS14-21	—	—	—	120	10	Amalgamated gravels	qtz vein	1	47.32905	0.30963	3.9105E–13	1.24E–14
HS14-22	—	—	—	145	10		qtz vein	1	32.27916	0.30216	2.4611E–13	7.82E–15

Table 2 *(continued)*

Sample name	Latitude (°N)	Longitude (°E)	Elevation (masl)	Depth (cm)	Loess cover (cm)	Type	Rock type	Thickness (cm)	Quartz mass (g)	9Be added (mg)	10Be/9Be	err
						Amalgamated gravels						
HS14-23	—	—	—	180	10	Amalgamated gravels	qtz vein	1	44.5818	0.31252	2.1556E−13	7.40E−15
HS14-24	—	—	—	210	10	Amalgamated gravels	qtz vein	1	32.82419	0.29890	1.2843E−13	4.28E−15
Terrace T4												
YR05-25	36.96225	104.41245	1,900	0		Cobble		3	44.07730	0.48900	1.05E−12	3.29E−14
YR05-27	36.96154	104.41180	1,887	0		Cobble		8	42.73050	0.49540	1.01E−12	3.09E−14
YR05-28	36.96057	104.41130	1,873	0		Cobble		4	45.13030	0.50510	1.09E−12	3.36E−14
YR05-29	36.96033	104.41110	1,870	0		Cobble		4	42.66140	0.50040	9.76E−13	3.00E−14
YR05-30	36.96028	104.41107	1,868	0		Cobble		3	48.35010	0.50360	1.27E−12	4.07E−14
YR05-31	36.96072	104.41181	1,879	0		Cobble		3	40.46220	0.49610	8.98E−13	2.72E−14
YR05-32	36.96087	104.41193	1,880	0		Cobble		3	33.48130	0.49410	8.13E−13	2.69E−14
YR05-33	36.96117	104.41210	1,884	0		Cobble		3	43.42760	0.49640	1.06E−12	3.21E−14
T4DP												
HS14-25	36.96229	104.41260	1,895	0	0	Amalgamated gravels	qtz vein	1	19.42213	0.29867	6.8210E−13	2.11E−14
HS14-26	—	—	—	25	20	Amalgamated gravels	qtz vein	1	14.58760	0.29863	3.9991E−13	1.25E−14
HS14-27	—	—	—	40	20	Amalgamated gravels	qtz vein	1	16.96731	0.2981	4.1592E−13	1.29E−14
HS14-28	—	—	—	60	20	Amalgamated gravels	qtz vein	1	21.21071	0.31311	1.0133E−13	3.24E−15
HS14-29	—	—	—	85	20	Amalgamated gravels	qtz vein	1	18.53141	0.29797	2.4168E−13	8.46E−15
HS14-30	—	—	—	100	20	Cobble	qtz vein	6	14.51491	0.31248	1.6799E−13	5.23E−15
HS14-31	—	—	—	110	20	Amalgamated gravels	qtz vein	1	48.34327	0.29768	4.5178E−13	1.34E−14
HS14-33	—	—	—	155	20	Amalgamated gravels	qtz vein	1	45.71112	0.30942	3.0275E−13	1.05E−14
HS14-35	—	—	—	230	20	Amalgamated gravels	qtz vein	1	44.64633	0.3106	1.3369E−13	5.27E−15

Note. Sample coordinates from handheld GPS and GoogleEarth. Shielding due to local topography is negligible, as it remains lower than 2%. Cobble size is in the range of 5 to 15 cm. Amalgamated quartz vein gravels range from 0.5 to 2 cm in size and a number between 30 and 50. Thickness is integrated vertically. ^{9}Be carrier is commercial solution with average ^{10}Be background of 3e–14 for surface samples (Inorganic Ventures CGBE1-1) and 2.5e–15 for subsurface samples (Scharlau). ^{10}Be/^{9}Be AMS ratio, measured at ASTER (CEREGE), is corrected for analytical blank. Be AMS standardization with NIST_27900 (https://hess.ess.washington.edu/math/v3/v3_age_in.html; Balco et al., 2008). Error on ^{10}Be concentration is quadratic sum of weighing errors, AMS (1–3%) and ^{9}Be carrier (2%). ^{10}Be exposure age is time-dependent exposure age with (Lal, 1991; Stone, 2000) scaling scheme calculated using the online exposure age calculator v3 formerly known as the CRONUS-Earth online exposure age calculator (https://hess.ess.washington.edu/math/v3/v3_age_in.html; Balco et al., 2008). Error is external uncertainty. Ages are calculated for surface samples with no erosion and no inheritance. Model ages for depth profiles assume no erosion and calculated with a local 10Be production rate of 15.12 at·g^{-1}·year^{-1}. Native ^{27}Al is determined by ICP-MS. Added ^{27}Al is commercial solution, Fluka with average ^{26}Al background of 5e–16. ^{26}Al/^{27}Al AMS ratio, measured at ASTER (CEREGE), is corrected for analytical blank. Al AMS standardization with SMALL11 (https://hess.ess.washington.edu/math/v3/v3_age_in.html; Balco et al., 2008). Error on ^{26}Al concentration is quadratic sum of weighing errors, AMS (1–3%), ^{27}Al carrier (2%), and ICP-MS measurement. ^{26}Al exposure age is time-dependent exposure age with (Lal, 1991; Stone, 2000) scaling scheme using the online exposure age calculator v3 formerly known as the CRONUS-Earth online exposure age calculator (https://hess.ess.washington.edu/math/v3/v3_age_in.html; Balco et al., 2008). Error is external uncertainty. Ages are calculated for surface samples with no erosion and no inheritance. Model ages for depth profiles assume no erosion and calculated with a local 26Al production rate of 99.94 at·g^{-1}·year^{-1}.

Among the 14 surface samples collected on T1, 6 samples were collected from the stretch of T1 located upstream of the fault and 8 from downstream of the fault (Figure 4). The ^{10}Be and ^{26}Al model exposure ages range from 5.7 ± 0.6 to 16.2 ± 1.6 kyr (Figure 11; Table 2). Although two samples (YR05-05 and YK05-09) are much older than all the others, with ages similar to the higher terrace (T2) just above, we calculate the mean age of Terrace T1 from the whole set of samples. Although the spread of ages is larger upstream than downstream, the upstream samples average age of 10.0 ± 4.0 kyr is close to the downstream samples average of 8.4±1.6 kyr, confirming that they belong to the same terrace (Figure 11). Overall, on T1 the mean exposure age, estimated as the average of the bounds at the 1-sigma level of the summed distribution (e.g., Daëron et al., 2004), is 9.1 ± 2.9 kyr.

Table 2
Analytical Results of 10Be and 26Al CRN Dating at Site S1 for 31 Surface Samples and 25 Depth Profile Samples

Sample name	10Be conc (at/g.qtz)	err (at/g.qtz)	10Be exposure ages (yrs)	err (yrs)	27Al native (mg)	27Al added (mg)	27Al total (mg)	26Al/27Al	err	26Al conc (at/g.qtz)	err (at/g.qtz)	26Al exposure ages (yrs)	err (yrs)
Terrace T0′													
YR05-22	17,1411	12,587	**102,94**	**1,113**			9.1625	2.69E−13	1.20E−14	85,6387	38,198	**8,300**	**943**
YR05-23	92,597	11,090	**5,603**	**805**			2.8893	5.07E−13	1.81E−14	469,988	16,782	**4,587**	**506**
YR05-24	60,714	10,472	**3,680**	**699**			3.0881	3.52E−13	1.78E−14	335,665	16,951	**3,281**	**380**
Terrace T1up													
YR05-02	188,653	16,381	**11,245**	**1,324**			4.7679	4.60E−13	1.68E−14	1,019,476	37,155	**9,813**	**1,087**
YR05-05	274,222	17,694	**16,256**	**1,665**			2.5250	1.73E−12	5.13E−14	1,532,069	45,529	**14,682**	**1,600**
YR05-06	115,384	15,297	**6,875**	**1,063**			4.2554	4.47E−13	1.69E−14	589,616	22,317	**5,667**	**629**
YR05-07	123,267	17,441	**7,471**	**1,213**			4.7642	4.03E−13	1.57E−14	673,760	26,226	**6,589**	**734**
YR05-08	120,237	15,514	**7,049**	**1,068**			3.6519	5.49E−13	1.84E−14	618,399	20,686	**5,849**	**641**
YR05-09	264,855	14,526	**15,688**	**1,515**			3.3548	1.43E−12	4.93E−14	1,361,928	47,053	**13,032**	**1,437**
Terrace T1down													
YR05-11-1	190,023	24,156	**11,845**	**1,778**			2.3593	5.78E−13	2.15E−14	975,371	36,207	**9,815**	**1,089**
YR05-13-1	155,092	24,128	**9,368**	**1,638**			2.4822	4.94E−13	2.02E−14	966,791	39,616	**9,432**	**1,059**
YR05-15-1	123,888	27,448	**7,532**	**1,775**			3.1295	2.91E−13	1.43E−14	745,687	36,748	**7,318**	**845**
YR05-16-1	124,246	17,791	**7,508**	**1,230**			2.2914	5.75E−13	1.91E−14	718,544	23,912	**7,008**	**768**
YR05-17-1	114,821	19,378	**6,942**	**1,296**			2.9439	3.72E−13	1.67E−14	649,047	29,185	**6,332**	**720**
YR05-18-1	173,375	17,373	**10,499**	**1,343**			2.2395	8.23E−13	2.46E−14	975,074	29,199	**9,535**	**1,037**
YR05-19-1	154,892	18,736	**9,390**	**1,360**			3.6285	3.80E−13	1.45E−14	773,275	29,602	**7,565**	**841**
YR05-21-1	120,241	32,097	**7,256**	**2,024**			2.3500	2.80E−13	1.47E−14	657,952	34,552	**6,406**	**749**
Terrace T2 DP													
HS14-3	284,193	10,601			0.5953	1.3124	1.9077	8.70E−13	3.62E−14	1,907,309	88,830		
HS14-4	191,440	7,115			0.5024	1.4409	1.9433	4.64E−13	1.89E−14	1,105,742	50,914		
HS14-5	123,530	6,285			0.3231	1.6628	1.9859	2.73E−13	1.42E−14	807,722	45,991		
HS14-6	97,805	4,575			0.4959	1.1723	1.6682	1.92E−13	1.45E−14	577,941	45,316		
HS14-7	83,234	3,070			1.6541	0.2721	1.9262	5.68E−13	2.09E−14	584,796	24,562		
HS14-8	91,151	3,367			1.6481	0.3624	2.0104	6.34E−13	2.94E−14	711,350	35,943		
HS14-9	93,143	3,441			1.5942	1.3590	2.9532	5.56E−13	2.18E−14	924,075	40,654		
Terrace T3													
YR05-34	624,120	14,178	**37,091**	**3,077**			6.4627	1.35E−12	3.86E−14	3,773,872	108,073	**36,456**	**4,004**
YR05-35	574,944	18,131	**34,827**	**2,988**			3.1221	2.01E−12	5.85E−14	3,306,972	96,274	**32,515**	**3,568**
YR05-36	650,017	19,136	**39,180**	**3,336**			4.0007	2.04E−12	5.99E−14	4,162,108	122,259	**40,843**	**4,504**
YR05-37	447,813	20,182	**27,389**	**2,508**			2.5300	2.37E−12	7.51E−14	2,474,960	78,526	**24,519**	**2,698**
YR05-38	596,153	20,095	**36,274**	**3,144**			1.9031	3.05E−12	8.76E−14	2,290,336	65,766	**22,501**	**2,455**
YR05-39	733,576	18,597	**44,427**	**3,727**			2.5053	3.47E−12	9.95E−14	3,135,588	89,967	**30,723**	**3,365**
T3 DP													
HS14-16	594,707	20,099			1.7593	1.5594	3.3186	9.73E−13	3.13E−14	3,743,182	141,984		
HS14-17	429,974	15,808			0.4072	1.6656	2.0727	1.24E−12	4.63E−14	3,189,318	138,233		
HS14-18	393,409	14,418			0.4894	1.5573	2.0466	9.23E−13	3.69E−14	2,511,055	113,719		
HS14-19	336,506	12,309			0.4712	1.4557	1.9268	9.22E−13	3.14E−14	2,318,514	93,312		
HS14-20	218,696	8,497			0.4503	1.5567	2.0070	5.29E−13	1.88E−14	1,388,735	57,708		
HS14-21	170,947	6,407			1.6156	0.6124	2.2280	9.48E−13	3.57E−14	1,004,135	42,910		
HS14-22	154,151	5,793			0.8366	1.1492	1.9858	7.14E−13	2.29E−14	996,437	37,943		
HS14-23	100,972	4,016			1.4619	0.6109	2.0728	4.96E−13	2.01E−14	519,348	23,503		
HS14-24	78,253	3,043			1.6487	0.3173	1.9660	3.94E−13	1.82E−14	528,525	26,723		
Terrace T4													
YR05-25	775,909	24,678	**46,121**	**3,974**			5.2568	1.38E−12	3.95E−14	3,663,714	105,039	**35,300**	**3,875**
YR05-27	783,828	25,789	**48,982**	**4,244**			5.5409	1.23E−12	4.30E−14	3,555,559	124,477	**35,996**	**4,021**
YR05-28	814,524	24,895	**49,771**	**4,269**			4.0852	1.88E−12	5.39E−14	3,792,295	108,894	**37,566**	**4,129**
YR05-29	765,256	26,091	**46,823**	**4,076**			2.7324	2.85E−12	8.16E−14	4,069,194	116,710	**40,449**	**4,452**
YR05-30	883,051	23,168	**53,760**	**4,536**			5.8020	1.40E−12	4.04E−14	3,756,586	108,163	**37,029**	**4,070**
YR05-31	735,813	27,273	**44,354**	**3,914**			2.3553	2.90E−12	8.38E−14	3,766,619	108,920	**36,845**	**4,050**
YR05-32	801,949	32,826	**48,356**	**4,355**			8.4637	7.36E−13	2.14E−14	4,154,367	120,751	**40,687**	**4,483**
YR05-33	806,962	25,426	**48,526**	**4,178**			2.3596	3.33E−12	1.03E−13	4,043,346	124,506	**39,467**	**4,365**

Table 2 *(continued)*

Sample name	10Be conc (at/g.qtz)	err (at/g.qtz)	10Be exposure ages (yrs)	err (yrs)	27Al native (mg)	27Al added (mg)	27Al total (mg)	26Al/27Al	err	26Al conc (at/g.qtz)	err (at/g.qtz)	26Al exposure ages (yrs)	err (yrs)
T4DP													
HS14-25	701,849	25,885			0.2709	1.76641	2.0373	2.08E–12	6.28E–14	4,997,736	193,026		
HS14-26	547,779	20,385			0.5835	1.43606	2.0196	1.23E–12	4.09E–14	3,885,815	152,683		
HS14-27	488,947	18,065			0.5889	1.44988	2.0388	1.21E–12	4.16E–14	3,302,592	133,228		
HS14-28	99,955	3,776			0.94845	1.0719	2.0203	2.72E–13	1.68E–14	587,472	38,084		
HS14-29	260,022	10,495			0.6361	1.47085	2.1069	6.58E–13	2.20E–14	1,702,499	67,075		
HS14-30	241,665	8,947			0.63449	1.3968	2.0313	4.86E–13	2.09E–14	1,547,479	73,832		
HS14-31	186,139	6,664			1.3398	0.59624	1.9361	1.37E–12	4.20E–14	1,239,192	45,383		
HS14-33	136,940	5,469			1.85664	0.0000	1.8566	9.79E–13	3.32E–14	887,820	34,953		
HS14-35	62,147	2,747			1.48332	0.6068	2.0901	3.63E–13	1.76E–14	382,701	20,088		

We did not collect samples from the surface of T2, as surficial rocks seem to have been moved around by local shepherds. Instead, we excavated a 2-m-deep pit (see position in Figure 4) and collected seven amalgamated samples from the surface (0 cm) down to a depth of 180 cm. Figure 10a shows the CRN concentrations with depth. Five samples out of seven fit a model assuming no erosion. The two deepest samples (HS14-8 and HS14-9) have higher CRN concentrations, with more discrepant ^{26}Al and ^{10}Be concentrations that may indicate a more complex exposure history, they are thus not included in the model calculation. The depth-profile models yield exposure ages for T2 of 16.0 ± 2.2 and 14.1±2.0 kyr for ^{10}Be and ^{26}Al, respectively. The average of these two estimates, calculated similarly to T1, is 15.0 ± 2.3 kyr (Figures 10 and 11).

We collected six samples on the surface of T3 on its highest part along the top of riser T3/T2 and excavated a 2.3-m-deep pit in the center of surface T3 to retrieve nine amalgamated gravel samples, from the surface down to a depth of 210 cm (Figure 4c). Overall, the distributions of ^{10}Be and ^{26}Al concentrations of the surface samples are close to the best model fitting the subsurface samples indicating minor surface modification (Figure 10b). The six surface sample ages scatter from 24 to 44 kyr with a mean age of 35 ± 6 kyr (Figure 11). Two samples (YR05-38 and 39) have discrepant ^{26}Al and ^{10}Be concentrations (>30%), leading us to exclude the ^{26}Al data for these two samples (Figure 11). Overall, the average of the surface ages (35 ± 6 kyr) are consistent with the average age of 36 ± 5 kyr modeled for the subsurface samples, leading to a Terrace T3 mean age, calculated like for Terrace T1, of 36 ± 6 kyr (Table 3; Figures 10b and 11).

On surface T4 we collected eight embedded cobbles and eight gravel amalgams in a pit from the surface down to 230 cm deep (Figures 4 and 10c). The pattern of ^{10}Be and ^{26}Al concentrations of the surface and subsurface samples is similar to that of Terrace T3 and thus indicates again minor surface modification (Figure 10c). The eight surface sample ages range from 37 to 53 kyr with a mean exposure age of 44 ± 6 kyr, excluding four discrepant ^{26}Al ages (Figure 11). Overall, the surface ages are consistent with the age of 44 ± 6 kyr modeled for the subsurface samples, leading to a mean age for terrace T4, calculated like for terrace T1, of 44 ± 7 kyr (Table 3; Figures 10c and 11).

In summary the 56 samples analyzed at Site S1, 31 from the surface and 25 from the subsubsurface constrain the ages of T1, T2, T3, and T4 to be 9 ± 3, 15 ± 2, 36 ± 6, and 44 ± 7 kyr, respectively. These ages are consistent with the emplacement scenario of the terraces: Their ages increase both with their heights above the present stream, and the closest terrace to the active stream is the youngest and the farthest to the east is the oldest, as expected for progressive left-lateral movement along the Haiyuan fault.

6. Interpretation

The terraces and fans along the southern front of the Hasi Shan are typical debris-flow deposits formed in response to changes in climate and particularly to the alternating phases of warm/wet and cold/dry

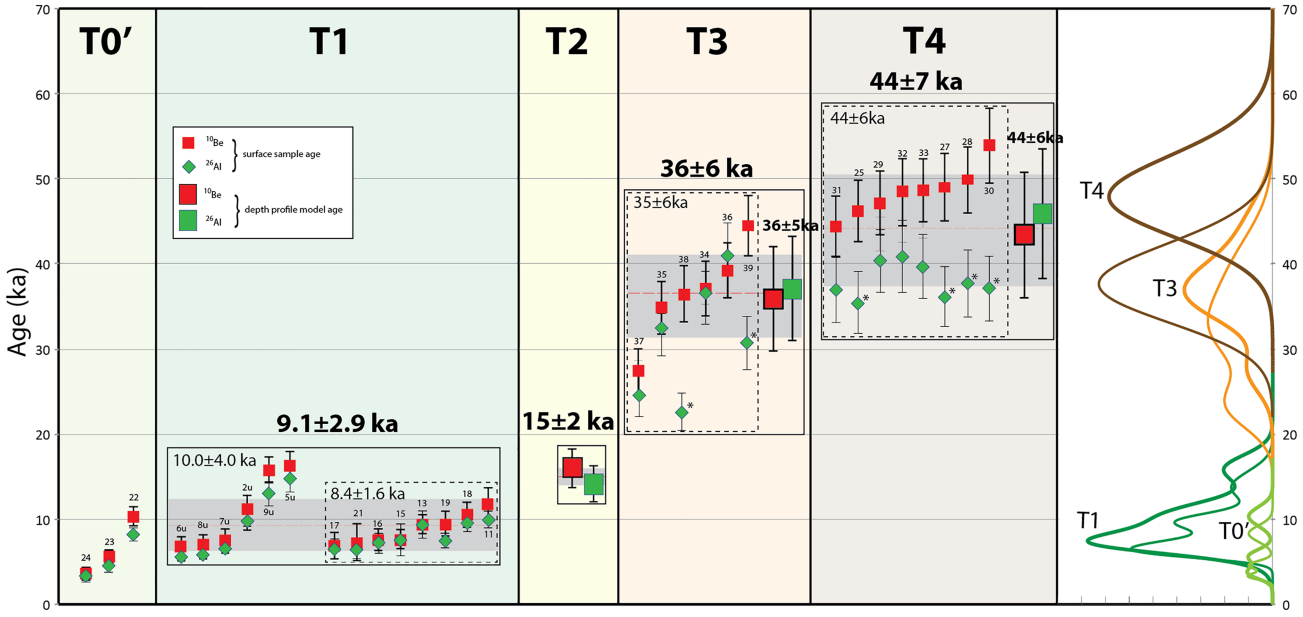

Figure 11. ^{10}Be and ^{26}Al CRN age distributions for five terraces at Site S1. For Terrace T1, *u* indicates samples collected upstream. To the right, summed Gaussian probability distributions for surface sample ages (^{10}Be bold and ^{26}Al thin). Details of mean ages calculations in the text and Table 3.

periods characterizing semiarid to arid areas of central Asia (Avouac et al., 1993; Hetzel et al., 2002; Meyer et al., 1998; Peltzer & Tapponnier, 1988; Van Der Woerd et al., 2002). In particular, the transitions from glacial to interglacial periods, like the last one from LGM (20 ka) to Holocene (10 ka), or the penultimate one from the penultimate glacial stage MIS-6 (150 ka) to the interglacial stage MIS-5e (125 ka), are widely recognized as major periods of sediment mobilization from the catchments (glaciated or unglaciated) to the piedmont, strongly impacting the landscape with wide and thick alluvial fan deposits (Chevalier et al., 2005; Peltzer & Tapponnier, 1988; Poisson & Avouac, 2004). In general, the climate changes following deglaciation are less important and spatially restricted with the formation of successive inset terraces (Bull, 1991; Meriaux et al., 2005; Van der Woerd et al., 2001; Van Der Woerd et al., 2002). Interestingly, at Site S1, the ages of the terraces follow the global climate changes as recorded in oxygen isotopes variations (e.g., Lisiecki & Raymo, 2005). The ages of T4, T3, and T2 correspond almost exactly to the MIS Stages 3c and 3a and the transition from MIS-2 to 1, with T1 corresponding to the first half of the Holocene, including the Holocene optimum (Rosenthal et al., 2013). The highest terraces T5 and T6, recognized all along the piedmont, may thus correspond to the various phases of the last major interglacial, namely, MIS-5e (125ka) and following (MIS-5a and 5c).

Table 3
Summary of Terrace Ages and Mean Ages Determined From the Combined ^{10}Be and ^{26}Al Surface and Depth Profile Ages

Terrace	^{10}Be age (years)	^{26}Al age (years)	mean ^{10}Be-^{26}Al age (years)
T1 up	10,764 ± 4,345	9,272 ± 3,889	10,018 ± 4,008
T1 down	8,793 ± 1,770	7,926 ± 1,445	8,353 ± 1,624
mean T1 (up+down)	9,637 ± 3,158	8,503 ± 2,724	9,050 ± 2,950
T2 DP	16,000 ± 2,223	14,100 ± 2,037	15,000 ± 2,300
T3 surface	36,531 ± 5,590	33,583 ± 6,934	35,057 ± 5,975
T3 DP	35,900 ± 4,721	37,100 ± 4,912	36,500 ± 4,900
T3 mean			36,000 ± 5,700
T4 surface	48,337 ± 2,803	39,362 ± 1,759	43,849 ± 5,975
T4 DP	43,300 ± 5,701	45,700 ± 6,007	44,500 ± 5,900
T4 mean			44,300 ± 5,800

As discussed above, along the Hasi Shan, one preeminent geomorphic feature in each catchment is the riser T3/T2, which is systematically higher than any other risers in that same catchment. The formation of this riser is bounded by the ages of Terraces T2 and T3, which are, respectively, 15 ± 2 and 36 ± 6 kyr. The latter age corresponds to MIS-3a, the last warm/wet period before the last Glacial Maximum (LGM, 20 ka), and the former age corresponds to the end of the dry/cold LGM and the return to the warm/wet period of the Holocene. Hence, we may assume that Terrace T3 has been abandoned and incised during the climate shift to the glacial period leading to the LGM. Then, during the transition from the dry glacial period to the wet and warm interglacial period, marked by increased runoff and erosion, the riser T3/T2 was reshaped together

with T2 emplacement. Less dramatic climatic changes during the Holocene may have only partially modified the risers with the lower terrace emplacements.

The morphology of alluvial deposits studied along the Hasi Shan fault section shows clear evidence of late Pleistocene and Holocene fault activity. However, deriving slip rates using offset alluvial terraces and associated ages requires carefulness (e.g., Behr et al., 2010; Peltzer et al., 1988; Sieh & Jahns, 1984; Van der Woerd et al., 2006; Weldon & Sieh, 1985). The main assumption relates to the association of in most cases a terrace deposit age with an offset that accumulated during and/or after the terrace formation. More commonly, the dated feature is the alluvial terrace, whereas the measured offset feature is an adjacent lower or upper terrace riser. Direct dating of a terrace riser would be very challenging, as risers are nonflat transient morphological features with different evolutions regarding to their location—upstream or downstream of the fault—right or left bank of the active stream (e.g., Cowgill, 2007; Gold et al., 2009; Meriaux et al., 2012). If the active stream is powerful enough, the active riser (i.e., the riser just above the active streambed) is continuously refreshed and laterally eroded, preventing any offset record. Therefore, a terrace riser becomes a passive marker and records cumulative offset only when the terrace at its base is abandoned, during a subsequent incision episode. In this case, the age of a terrace riser is defined by the surface exposure age of the lower terrace, hence yielding a minimum age for the riser and a maximum slip rate (e.g., Van Der Woerd et al., 1998, 2002).

These considerations naturally only apply on the long term in case of intermittent stream in arid areas. Strong floods in the active river bed occurring only from time to time, coseismic offset might be preserved over a certain period of time. This is probably the case at our sites. Indeed, the lower riser (T1/T0) still preserves an offset of about 6 m (5.8 ± 0.5 m) that we link to the last large earthquake occurring along this segment of the Haiyuan fault, namely, the 1920 magnitude M8 earthquake (Ren et al., 2016). This observation is consistent with the average recurrence time for such large earthquake that has been estimated to reach several centuries (600–650 years; Liu-Zeng et al., 2007). If T0 remains the active riverbed for the next half millennia, it is highly likely that the 6-m offset will be eroded away until the next large event.

Using the "lower terrace" assumption and only considering the offset measurements and CRN dating at Site S1, we used either the smaller or the larger offsets and related uncertainties to determine, respectively, the lower and upper bounds of the slip rate. In the case of the riser T2/T1, the same value was used in both calculations. In each case, the slip rate was determined following a Bayesian approach following Styron (2015) with 5,000 iterations. Uncertainties for offset were defined as a preferred value associated to a minimum and maximum possible offset. The probability of occurrence of offset value during the Bayesian process decreases linearly from the preferred value to zero at the extrema. For the ages, uncertainties are considered as following a normal distribution with a standard deviation derived from the age calculation. Hence, the minimum and maximum slip rates along the Hasi Shan fault strand, based on our measurement at Site S1, are, respectively, 2.7 and 3.0 mm/year (Table 1 for summary of offsets and associated terrace ages; see also Figure S2). However, as mentioned previously, offset measurements at Site S1 yield only minimum offset values, as part of the cumulative displacement is probably missing upstream of the fault. Hence, the rates derived only from offset measurements at Site S1 yield minimum values of slip rates.

We measured offsets at three other sites (Sites S2, S3, and S4) where we identified patterns of inset terraces similar to Site S1, using riser T3/T2 as a stratigraphic and chronological reference (Table 1). We found good consistency of offsets between Sites S1 and S2. At Site S3, the T3/T2 offset is consistent with the upper bound of T3/T2 offset at site S1. In addition, the T1/T0 and T2/T1 offsets at Site S3 are larger than T1/T0 and T2/T1 at Site S1. As mentioned above, the main stream at Site S3 is deeply incised. Therefore, we can assume that the active river does not reach the terrace or the riser anymore, hence protecting the terraces from erosion and preserving them. At Site S4, T2/T1, T3/T2, and T4′/T4 offsets are consistent with the upper bounds of the offsets at Site S1. The offset T4/T3 at Site S4, although consistent with all other offsets measured at the different sites, is larger than similar offset at Site S1, however, emphasizing that Site S1 might yield only minimum offsets. Thus, using terrace matching from site to site, we associated the ages of terraces at Site S1 with the matching terraces of the other sites, and derived slip rates including all the offsets measurements. Because for the different offset risers at each site the determination of offset is not necessarily unique, in our determination of slip rate we have considered two end-member models: In one case we have systematically chosen the smallest offset determinations, and in the other case we

chose the largest offsets. In both cases we also have considered uncertainties attached to each offset and age in our estimate of the slip rate. Hence, as for site S1, we followed a Bayesian approach and used the slip-rate calculator by Styron (2015) with 5,000 iterations. Uncertainties were processed as described for Site S1 alone. It yields maximum and minimum slip rates for the main strand of the Haiyuan fault, south of the Hasi Shan, which are, respectively, 3.32 ± 0.21 and 3.1 ± 0.2 mm/year over 50 kyr (Figure 12). It is worth noting that these two slip rates are actually undistinguishable, emphasizing the need to correctly incorporate uncertainties in such calculation.

Our average slip rate of 3.2 ± 0.2 mm/year compares well with the lower bound of slip rates obtained by other groups along adjacent fault sections, although these rates are mostly determined over the Holocene, and the quality of rate determination is variable depending on each study (Table S1). Immediately east of the Hasi Shan, Li et al. (2009) derived a Late Quaternary slip rate of 5.0 ± 2.5 mm/year from offset stream valleys and ^{14}C dating (Figure 1). Further east along the Haiyuan fault, the same authors derived Late Quaternary slip rates from offset terraces and stream valleys, and ^{14}C dating (Figure 1) of 4.2 ± 0.8 and 4.5 ± 0.7 mm/year. Along the same segments east of the Hasi Shan, Zhang et al. (1988) derived an average Holocene slip rate of 8 ± 2 mm/year from offset streams and ^{14}C dating, with lower bounds between 3.4 ± 0.7 and 4.1 ± 0.4 mm/year.

Short-term slip rates derived from geodesy also show consistent values in the vicinity of the Hasi Shan: GPS data yield slip rates of 2.0 to 3.2 mm/year (Gan et al., 2007) and 3.6 ± 1.4 to 4.2 ± 1.5 mm/year (Zheng et al., 2013). Similarly, InSAR studies yield slip rates of 4.3 ± 1.0 mm/year (Daout et al., 2016), 5.0 ± 1.0 mm/year (Jolivet et al., 2012), and 6 ± 2 mm/year (Cavalié et al., 2008) just west of the Hasi Shan.

In addition to the horizontal slip rate, evidence for vertical motion along the Hasi Shan section of the Haiyuan fault is also visible. At Site S1, the upstream and downstream parts of Terrace T1 on the west bank of the active stream are separated by a southwest facing fault scarp about 3.6 ± 0.3 m high (Figure 5). Just above the fault trace, T1 is subhorizontal (slope ~2°) for a few tens of meters, whereas the average slope of the terrace is 5–6°. This bulge is likely to be a local effect related to the geometry of the shallow fault that might become steeper when it comes close to the surface. As presented earlier, we constrained an exposure age of 9.1 ± 2.9 kyr for T1. Hence, we can derive an uplift rate of 0.4 ± 0.2 mm/year. This uplift rate is consistent with the fact that the fault strike veers southward in the vicinity of the Hasi Shan, from 104°N west of the range to 120°N east of the range. This drastic shift of 16° over a distance of 35 km leads to oblique slip mixing fault-parallel shearing and fault-normal shortening, resulting in a transpressional structure with basement thrusting over Quaternary deposits (Figure 13). This uplift of the Hasi Shan would be consistent with the shortening observed by geodetic studies across the Haiyuan fault system (Daout et al., 2016; Gan et al., 2007). This combination of strike-slip and thrust motion defines the Hasi Shan as a significant restraining bend along the Haiyuan fault, similar to the Mont Lebanon along the Levant left-lateral strike-slip fault (Daëron et al., 2007; Goren et al., 2015), and to the "Big Bend" of the San Andreas right-lateral strike-slip fault (Eberhart-Phillips et al., 1990), although at a smaller scale.

7. Discussion

Complex fault systems with splays or intersecting faults have been documented to show potential slip variations with time, as slip might switch from one fault to the other (e.g., (Bennett et al., 2004; Dolan et al., 2016; Friedrich et al., 2003; Gold et al., 2017)). The central Haiyuan fault, with its two subparallel fault strands, the main central Haiyuan fault and the Zhongwei fault, may display such behavior. However, the geological slip rate along the Haiyuan fault determined in this study for an unusually long time period, from Holocene (9 kyr) to mid-Pleistocene (50 kyr), indicates a fairly constant slip rate with time. At our reference site, these rates are, respectively, 1.9 ± 0.6, 2.7 ± 0.5, 2.0 ± 0.25, and 3.5 ± 0.4 mm/yr over time periods of 9.1 ± 2.9, 15 ± 2, 36 ± 6, and 44 ± 6 kyr. In addition, although without direct dating in this study and based on similar reasoning as we used for other markers about the correlation between large risers and change in climatic condition, we could infer that T6, the highest terrace remnant in each catchment, which is offset about 500–600 m, formed during the penultimate glacial-interglacial transition (MIS-6 to 5e at 150–125 ka). Such assumption yields a slip rate of 4 ± 0.7 mm/year in keeping with the other rates.

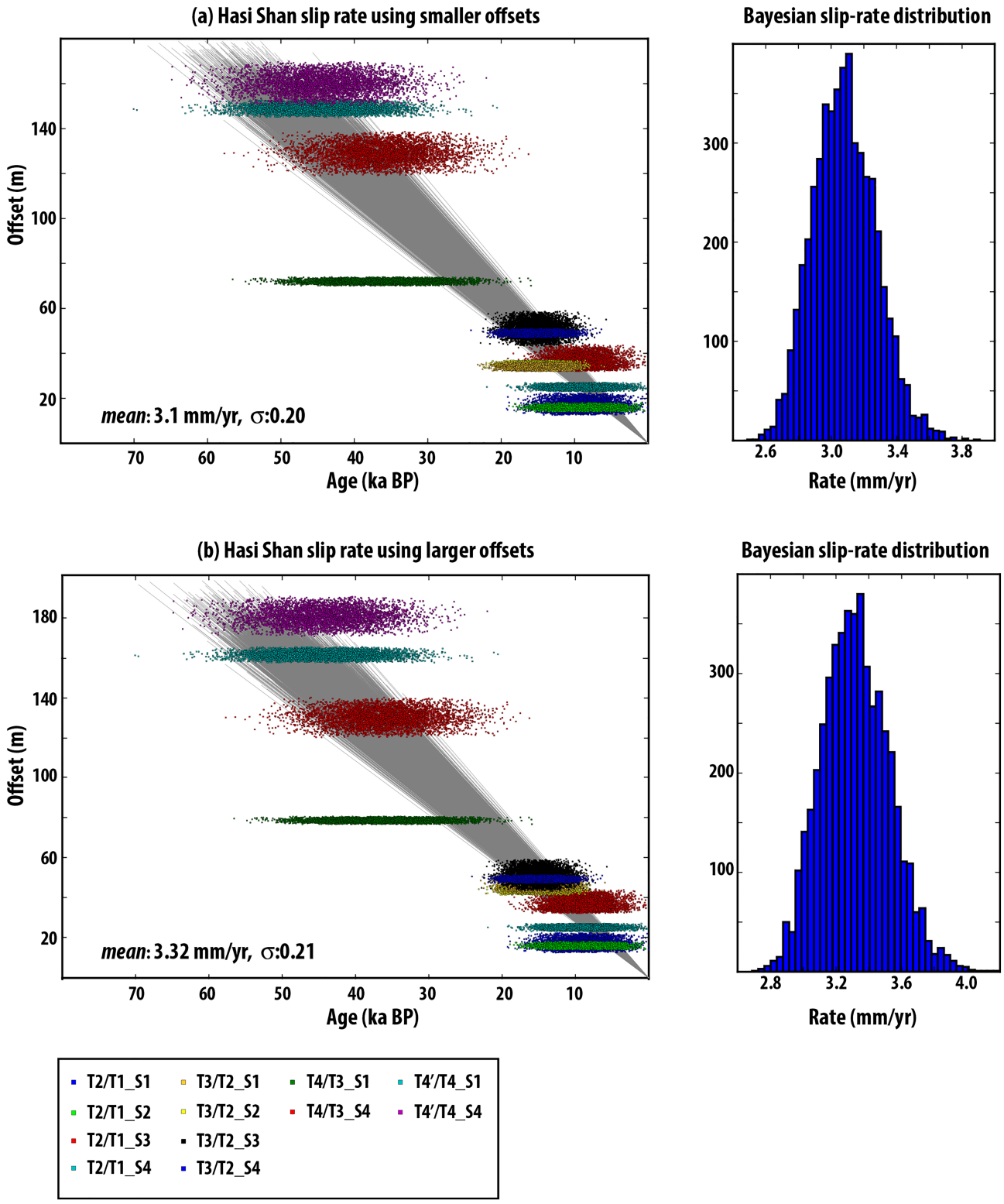

Figure 12. Slip rate estimates using a Bayesian approach (Styron, 2015). (a and b) Slip rates determined using minimum and maximum offset bounds outlined by piercing lines at sites S1 to S4, respectively. Uncertainty for slip rate is 1-sigma (see also Table 1).

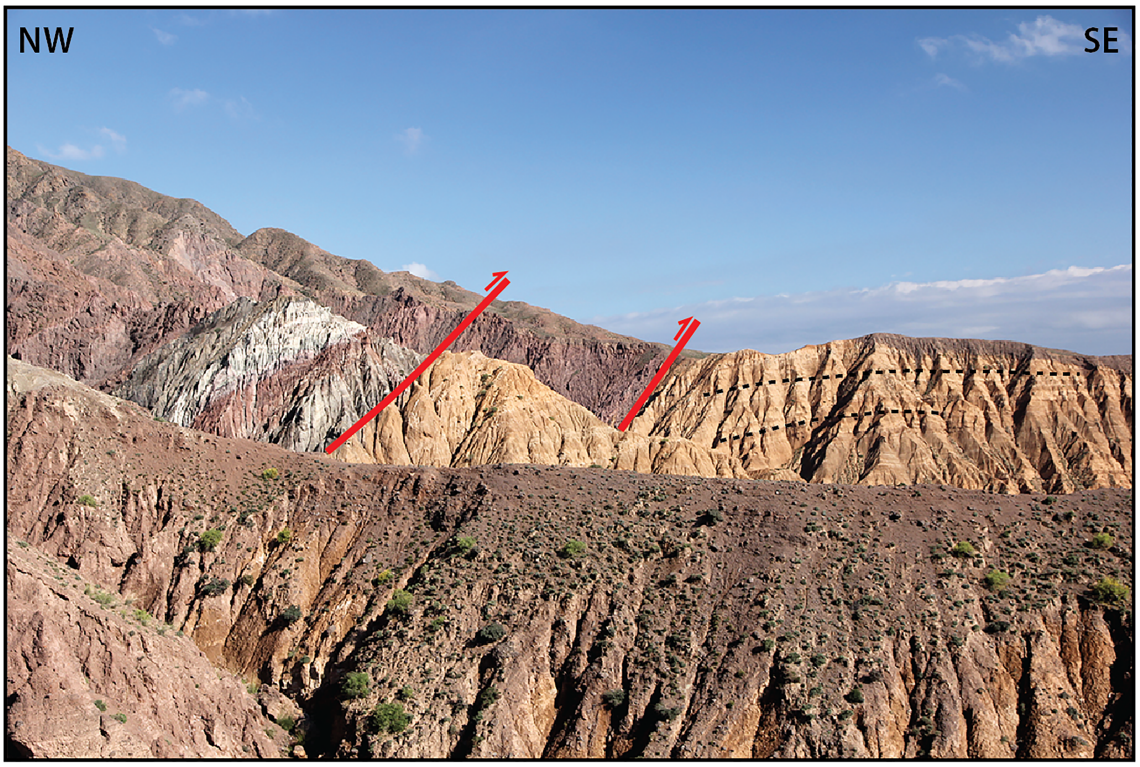

Figure 13. SE looking view of Hasi Shan southern front. Purple-white palaeozoic sandstones and conglomerate are overthrusting orange-colored tertiary sandstones. Dashed lines indicate the bending of the tertiary sandstones.

Hence, our results suggest that the slip rate does not vary significantly over long periods of time that can extend at least over few tens of thousands of years. Consistency of the geological slip rates with slip rates derived from short-term spatial geodesy also suggests that even at the time scale of the earthquake cycle, the slip rate is likely to not show large variations (Hetzel et al., 2019; Meade et al., 2013).

Overall, despite some inconsistencies between different rates published by different groups (see summary in previous sections and Table S1), a coherent picture emerges from the various slip-rate determinations, including the one proposed in this work: The horizontal slip rate along the Haiyuan fault is faster along the western section of the fault than along the central section. Even along the central section, the eastern part of the fault, along the Hasi Shan, seems to be slower than the western part. Such apparent fading of the horizontal slip rate along the main strand of the Haiyuan fault has been used as an argument to suggest that localized deformation progressively disappears, when moving eastward along the Haiyuan fault, to the benefit of distributed deformation (Duvall & Clark, 2010). Alternatively, we suggest that this apparent decrease of localized deformation results from the spread of the finite deformation associated to the Haiyuan fault over multiple fault strands in the area of the Hasi Shan. Such distribution of deformation over several faults makes it more difficult to constrain individual rate with GPS due to superimposition of the elastic contribution of each fault over large distances (see, for instance, similar discussion about rate distribution along the southern San Andreas fault system and Eastern California Shear Zone; e.g., Bennett et al., 2004; van der Woerd et al., 2006).

As described earlier in this work, the main Hasi Shan fault strand is moving horizontally at 3.2 ± 0.2 mm/year. At least one secondary strike-slip fault strand cuts across the southern Hasi Shan bajada (Figures 2 and 3). This fault, which separates lower, to the north, from upper, to the south, Pliocene conglomerates (Pan et al., 2004), is clearly active as it cuts and offsets a surface that can be traced upstream to be T1 at Site S1 (Figure 3b). Two additional secondary strands are also visible to the north. One strikes across the middle of the Hasi Shan range, underlined by a gouge zone separating Silurian metasediments to the south from Devonian conglomerates to the north at the base of steep facets. The other one follows the

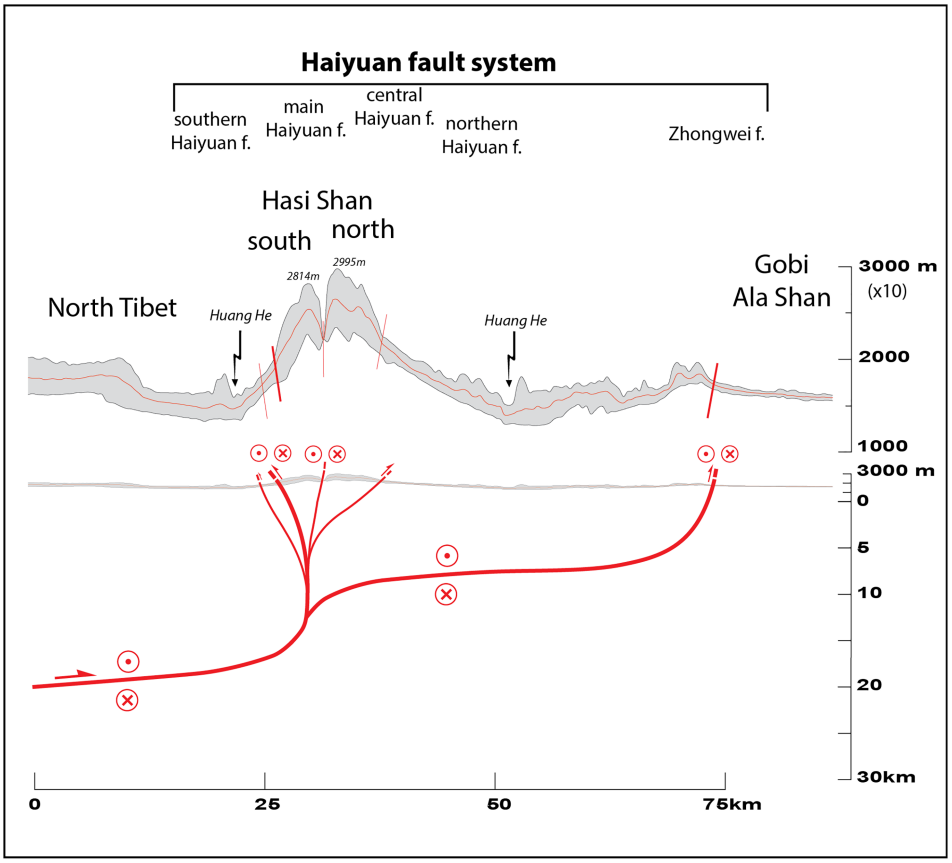

Figure 14. General cross section of entire Haiyuan fault system showing possible fault strands geometry and link at depth (adapted from Gaudemer et al., 1995; Daout et al., 2016). Upper panel shows vertical topography exaggerated 10 times.

northern rim of the northern Hasi Shan range, as a steep thrust between the deformed Devonian conglomerate overthrusting steeply south dipping Miocene conglomerates, itself overthrusting Pliocene sediments (Figure 2). Although the quantification of slip rate for these secondary structures goes beyond this work, their clear traces in the morphology and across Quaternary deposits indicate that they are active faults. Indeed, they are indicated as such on the regional geological map (Pan et al., 2004). Based on comparison between the slip rate we obtain along the Hasi Shan and the slip rates available both west and east of the Hasi Shan (Figure 1; Table S1), together these secondary faults might accommodate up to 1 mm/year. Thus, put together, the different fault strands of the Haiyuan fault at the Hasi Shan yield a minimum total slip rate of 4 to 5 mm/year, not even accounting for the vertical deformation. This rate should then be added up with the horizontal slip rate estimated for the Zhongwei fault strand, ranging between 1 and 2 mm/year, which is accommodating another part of the total budget of deformation across the Haiyuan fault system (Figures 1 and 14), yielding to a total slip rate across the Haiyuan fault, at the longitude of the Hasi Shan, of 5 to 7 mm/year. This is consistent with the total slip rate of 8.0 $\pm$ 1.3 mm/year estimated from geodesy across the entire Haiyuan fault system (Daout et al., 2016), and it demonstrates that the amount of slip accommodated by localized faults along the Haiyuan fault system does not significantly decrease eastward when the fault system is fully considered.

Our result shows the importance of encompassing the full geometry of the fault system when considering the rate of deformation, as ignoring slip distributed on additional fault strands to the main strand might lead to erroneous conclusion of major slip-rate variation along strike for a single fault, which is indeed hardly sustainable when considering realistic physical deformation processes.

Acknowledgments

We thank the associate editor and an anonymous reviewer for their insightful comments that greatly improve this manuscript. We are grateful to René Boutin at Laboratoire d'Hydrologie et Géochimie de la Surface and ASTER Team (G. Aumaître, D. Bourlès, and K. Keddadouche) at ASTER-CEREGE for ICP-AES and AMS measurements, respectively. Part of this work was supported by INSU-CNRS, France, and the University of Strasbourg, J. Van der Woerd for the Al and Be concentration analyses at LHyGeS and IPGS, and for $^{10}Be/^{9}Be$ and $^{26}Al/^{27}Al$ ratios measurements on the Aster AMS facility (GEREGE, Aix-en-Provence, France) supported by INSU-CNRS and IRD. We thank Yang Ye for his help with the chi-square modeling of the depth profile data and A. S. Mériaux for her help with error propagation and mean age calculations. Part of this work has been supported by the CNRS PICS program France-Chine. All slip-rate data discussed in the paper, but the ones derived in this study, are extracted from the published literature listed in the reference list. Pleiades imagery is available for purchase from Airbus industry (https://www.intelligence-airbusds.com/en/8692-pleiades). This is IPGP contribution 4090.

References

Anderson, R., Repka, J., & Dick, G. (1996). Dating depositional surfaces using in situ produced cosmogenic radionuclides. *Geology*, *24*, 47–51.

Avouac, J. P., Tapponnier, P., Bai, M., You, H., & Wang, G. (1993). Active thrusting and folding along the northern Tien Shan and late Cenozoic rotation of the Tarim relative to Dzungaria and Kazakhstan. *Journal of Geophysical Research*, *98*(B4), 6755–6804.

Balco, G. (2017). Production rate calculations for cosmic-ray-muon-produced ^{10}Be and ^{26}Al benchmarked against geological calibration data. *Quaternary Geochronology*, *39*, 150–173. https://doi.org/10.1016/j.quageo.2017.02.001

Balco, G., Stone, J. O., Lifton, N. A., & Dunai, T. J. (2008). A complete and easily accessible means of calculating surface exposure ages or erosion rates from 10Be and 26Al measurements. *Quaternary Geochronology*, *3*(3), 174–195.

Behr, W. M., Rood, D. H., Fletcher, K., Guzman, N., Finkel, R., Hanks, T., et al. (2010). Uncertainties in slip-rate estimates for the Mission Creek strand of the southern San Andreas fault at Biskra Palms Oasis, southern California. *GSA Bulletin*, *122*(9-10), 1360–1377. https://doi.org/10.1130/B30020.1

Bennett, R. A., Friedrich, A. M., & Furlong, K. P. (2004). Codependent histories of the San Andreas and San Jacinto fault zones from inversion of fault displacement rates. *Geology*, *32*(11), 961–964.

Borchers, B., Marrero, S., Balco, G., Caffee, M., Goehring, B., Lifton, N., et al. (2016). Geological calibration of spallation production rates in the CRONUS-Earth project. *Quaternary Geochronology*, *31*, 188–198. https://doi.org/10.1016/j.quageo.2015.01.009

Braucher, R., Brown, E., Bourlès, D., & Colin, F. (2003). In situ produced 10Be measurements at great depths: Implications for production rates by fast muons. *Earth and Planetary Science Letters*, *211*(3-4), 251–258.

Braucher, R., Merchel, S., Borgomano, J., & Bourlès, D. L. (2011). Production of cosmogenic radionuclides at great depth: A multi element approach. *Earth and Planetary Science Letters*, *309*, 1–9.

Bull, W. B. (1991). *Geomorphic responses to climatic change*. New York: Oxford University Press.

Burchfiel, B. C., Peizhen, Z., Yipeng, W., Weiqi, Z., Fangmin, S., Qidong, D., et al. (1991). Geology of the Haiyuan Zone, Ningxia-Hui Autonomous Region, China, and its relation to the evolution of the northeastern margin of the Tibetan Plateau. *Tectonics*, *10*(6), 1091–1110.

Cavalié, O., Lasserre, C., Doin, M.-P., Peltzer, G., Sun, J., Xu, X., & Shen, Z.-K. (2008). Measurement of interseismic strain across the Haiyuan fault (Gansu, China), by InSAR. *Earth and Planetary Science Letters*, *275*(3), 246–257.

Chevalier, M. L., Ryerson, F. J., Tapponnier, P., Finkel, R. C., Van der Woerd, J., Li, H. B., & Liu, Q. (2005). Slip-rate measurements on the Karakorum Fault may imply secular variations in fault motion. *Science*, *307*(5708), 411–414. https://doi.org/10.1126/science.1105466

Cowgill, E. (2007). Impact of riser reconstructions on estimation of secular variation in rates of strike–slip faulting: Revisiting the Cherchen River site along the Altyn Tagh Fault, NW China. *Earth and Planetary Science Letters*, *254*(3-4), 239–255.

Daëron, M., Benedetti, L., Tapponnier, P., Sursock, A., & Finkel, R. C. (2004). Constraints on the post ~25-ka slip rate of the Yammoûneh fault (Lebanon) using in situ cosmogenic ^{36}Cl dating of offset limestone-clast fans. *Earth and Planetary Science Letters*, *227*, 105–119.

Daëron, M., Klinger, Y., Tapponnier, P., Elias, A., Jacques, E., & Sursock, A. (2007). 12,000-year-long record of up to 14 paleo-earthquakes on the Yammoûneh fault (Levant fault system). *Bulletin of the Seismological Society of America*, *97*(3), 749–771.

Daout, S., Jolivet, R., Lasserre, C., Doin, M. P., Barbot, S., Tapponnier, P., et al. (2016). Along-strike variations of the partitioning of convergence across the Haiyuan fault system detected by InSAR. *Geophysical Journal International*, *205*(1), 536–547. https://doi.org/10.1093/gji/ggw028

Delmas, M., Calvet, M., Gunnell, Y., Voinchet, P., Manel, C., Braucher, R., et al. (2018). Terrestrial 10Be and electron spin resonance dating of fluvial terraces quantifies quaternary tectonic uplift gradients in the eastern Pyrenees. *Quaternary Science Reviews*, *193*, 188–211. https://doi.org/10.1016/j.quascirev.2018.06.001

Deng, Q., Chen, S., Song, F., Zhu, S., Wang, Y., Zhang, W., et al. (1986). Variations in the geometry and amount of slip on the Haiyuan (Nanxihaushan) fault zone, China and the surface rupture of the 1920 Haiyuan earthquake. *Earthquake Source Mechanics*, *37*, 169–182.

Deng, Q., Sung, F., Zhu, S., Li, M., Wang, T., Zhang, W., et al. (1984). Active faulting and tectonics of the Ningxia-Hui autonomous region, China. *Journal of Geophysical Research*, *89*, 4427–4445.

Dolan, J. F., McAuliffe, L. J., Rhodes, E. J., McGill, S. F., & Zinke, R. (2016). Extreme multi-millennial slip rate variations on the Garlock fault, California: Strain super-cycles, potentially time-variable fault strength, and implications for system-level earthquake occurrence. *Earth and Planetary Science Letters*, *446*, 123–136. https://doi.org/10.1016/j.epsl.2016.04.011

Duvall, A. R., & Clark, M. K. (2010). Dissipation of fast strike-slip faulting within and beyond northeastern Tibet. *Geology*, *38*(3), 223–226.

Eberhart-Phillips, D., Lisowski, M., & Zoback, M. D. (1990). Crustal strain near the big bend of the San Andreas fault: Analysis of the Los Padres-Tehachapi trilateration networks, California. *Journal of Geophysical Research*, *95*(B2), 1139–1153. https://doi.org/10.1029/JB095iB02p01139

Friedrich, A. M., Wernicke, B. P., Niemi, N. A., Bennett, R. A., & Davis, J. L. (2003). Comparison of geodetic and geologic data from the Wasatch region, Utah, and implications for the spectral character of Earth deformation at periods of 10 to 10 million years. *Journal of Geophysical Research*, *108*(B4), 2199. https://doi.org/10.1029/2001JB000682

Gan, W., Zhang, P., Shen, Z. K., Niu, Z., Wang, M., Wan, Y., et al. (2007). Present-day crustal motion within the Tibetan Plateau inferred from GPS measurements. *Journal of Geophysical Research*, *112*, B08416. https://doi.org/10.1029/2005JB004120

Gaudemer, Y., Tapponnier, P., Meyer, B., Peltzer, G., Shunmin, G., Zhitai, C., et al. (1995). Partitioning of crustal slip between linked active faults in the eastern Qilian Shan, and evidence for a major seismic gap, the 'Tianzhu Gap', on the western Haiyuan fault, Gansu (China). *Geophysical Journal International*, *120*(3), 599–645.

Gold, P., Behr, W. M., Rood, D., Sharp, W. D., Rockwell, T. K., Kendrick, K., & Salin, A. (2015). Holocene geologic slip rate for the Banning strand of the soutehrn San Andreas fault, southern California. *Journal of Geophysical Research: Solid Earth*, *120*, 5639–5663. https://doi.org/10.1002/2015JB012004

Gold, R. D., Cowgill, E., Arrowsmith, J. R., & Friedrich, A. M. (2017). Pulsed strain release on the Altyn Tagh fault, northwest China. *Earth and Planetary Science Letters*, *459*, 291–300. https://doi.org/10.1016/j.epsl.2016.11.024

Gold, R. D., Cowgill, E., Arrowsmith, J. R., Gosse, J., Chen, X., & Wang, X. F. (2009). Riser diachroneity, lateral erosion, and uncertainty in rates of strike-slip faulting: A case study from Tuzidun along the Altyn Tagh Fault, NW China. *Journal of Geophysical Research*, *114*, B04401. https://doi.org/10.1029/2008JB005913

Goren, L., Castelltort, S., & Klinger, Y. (2015). Modes and rates of horizontal deformation from rotated river basins: Application to the Dead Sea fault system in Lebanon. *Geology*, *43*(9), 843–846.

Gosse, J. C., & Phillips, F. M. (2001). Terrestrial in situ cosmogenic nuclides: Theory and application. *Quaternary Science Reviews*, *20*(14), 1475–1560.

Guilbaud, C., Simoes, M., Barrier, L., Laborde, A., Van der Woerd, J., Li, H., et al. (2017). Kinematics of active deformation across the Western Kunlun mountain range (Xinjiang, China) and potential seismic hazards within the southern Tarim Basin. *Journal of Geophysical Research: Solid Earth*, *122*, 10,398–10,426. https://doi.org/10.1002/2017JB014069

Hancock, G., Anderson, R., Chadwick, O., & Finkel, R. (1999). Dating fluvial terraces with ^{10}Be and ^{36}Al profiles: Application to the Wind River, Wyoming. *Geomorphology*, *27*, 41–60.

Hetzel, R. (2013). Active faulting, mountain growth, and erosion at the margings of the Tibetan plateau constrained by in situ produced cosmogenic nuclides. *Tectonophysics*, *582*, 1–24. https://doi.org/10.1016/j.tecto.2012.10.027

Hetzel, R., Hampel, A., Gebbeken, P., Xu, Q., & Gold, R. D. (2019). A constant slip rate for the western Qilian Shan frontal thrust during the last 200 ka consistent with GPS-derived and geological shortening rates. *Earth and Planetary Science Letters*, *509*, 100–113. https://doi.org/10.1016/j.epsl.2018.12.032

Hetzel, R., Niedermann, S., Tao, M., Kubik, P. W., Ivy-Ochs, S., Gao, B., & Strecker, M. R. (2002). Low slip rates and long-term preservation of geomorphic features in Central Asia. *Nature*, *417*(6887), 428–432. https://doi.org/10.1038/417428a

Hidy, A. J., Gosse, J. C., Pedesson, J. L., Mattern, J. P., & Finkel, R. C. (2010). A geologically constrained Monte Carlo approach to modelling exposure ages from profiles of cosmogenic nucledes: An example from Lees Ferry, Arizona. *Geochemistry, Geophysics, Geosystems*, *11*, Q0AA10. https://doi.org/10.1029/2010GC003084

Jiang, W., Han, Z., Guo, P., Zhang, J., Jiao, Q., Kang, S., & Tian, Y. (2017). Slip rate and recurrence intervals of the east Lenglongling fault constrained by morphotectonics: Tectonic implications for the northeastern Tibetan Plateau. *Lithosphere*, *9*(3), 417–430. https://doi.org/10.1130/L597.1

Jolivet, R., Lasserre, C., Doin, M. P., Guillaso, S., Peltzer, G., Dailu, R., et al. (2012). Shallow creep on the Haiyuan fault (Gansu, China) revealed by SAR interferometry. *Journal of Geophysical Research*, *117*, B06401. https://doi.org/10.1029/2011JB008732

Kohl, C., & Nishiizumi, K. (1992). Chemical isolation of quartz for measurement of in-situ-produced cosmogenic nuclides. *Geochimica et Cosmochimica Acta*, *56*(9), 3583–3587.

Lal, D. (1991). Cosmic ray labeling of erosion surfaces: In situ nuclide production rates and erosion models. *Earth and Planetary Science Letters*, *104*(2-4), 424–439.

Lasserre, C., Gaudemer, Y., Tapponnier, P., Meriaux, A. S., Van der Woerd, J., Yuan, D. Y., et al. (2002). Fast late Pleistocene slip rate on the Leng Long Ling segment of the Haiyuan fault, Qinghai, China. *Journal of Geophysical Research*, *107*(B11), 2276. https://doi.org/10.1029/2000JB000060

Lasserre, C., Morel, P. H., Gaudemer, Y., Tapponnier, P., Ryerson, F. J., King, G. C. P., et al. (1999). Post-glacial left slip-rate and past occurrence of M$\underline{>}$8 earthquakes on the western Haiyuan fault, Gansu, China. *Journal of Geophysical Research*, *104*(B8), 17,633–17,651. https://doi.org/10.1029/1998JB900082

Le Béon, M., Klinger, Y., Al-Qaryouti, M., Meriaux, A. S., Finkel, R. C., Elias, A., et al. (2010). Early Holocene and late Pleisotoce slip rate of the southern Dead Sea fault determined by 10Be cosmogenic dating of offset alluvial deposits. *Journal of Geophysical Research*, *115*, B11414. https://doi.org/10.1029/2009JB007198

Le Béon, M., Klinger, Y., Meriaux, A. S., Al-Qaryouti, M., Finkel, R. C., Mayyas, O., & Tapponnier, P. (2012). Quaternary morphotectonic mapping of the Wadi Araba and implications for the tectonic activity of the southern Dead Sea fault. *Tectonics*, *31*, TC5003. https://doi.org/10.1029/2012TC003112

Li, C., Zhang, P. Z., Yin, J., & Min, W. (2009). Late Quaternary left-lateral slip rate of the Haiyuan fault, northeastern margin of the Tibetan Plateau. *Tectonics*, *28*, TC5010. https://doi.org/10.1029/2008TC002302

Li, H., Van Der Woerd, J., Tapponnier, P., Klinger, Y., Qi, X., Yang, J., & Zhu, Y. (2005). Slip rate on the Kunlun fault at Hongshui Gou, and recurrence time of great events comparable to the 14/11/2001, Mw~7.9 Kokoxili earthquake. *Earth and Planetary Science Letters*, *237*, 285–299. https://doi.org/10.1016/j.epsl.2005.05.041

Li, X., Li, C., Pierce, I. K., Zhang, P. Z., Zheng, W., Dong, J., et al. (2019). New slip rates for the Tianjinshan fault using optically stimulated luminescence, GPS, and paleoseismic data, NE Tibet, China. *Tectonophysics*, *755*, 64–74. https://doi.org/10.1016/j.tecto.2019.02.007

Li, X., Li, C., Wesnousky, S., Zhang, P. Z., Zheng, W. J., Pierce, I. K., & Wang, X. G. (2017). Paleoseismology and slip rate of the western Tianjingshan fault of NE Tibet, China. *Journal of Asian Earth Sciences*, *146*, 304–316. https://doi.org/10.1016/jseaes.2017.04.031

Lisiecki, L. E., & Raymo, M. E. (2005). A Pliocene-Pleistocene stack of 57 globally distributed benthic δ^{18}O records. *Paleoceanography*, *20*, PA1003. https://doi.org/10.1029/2004PA001071

Liu, J., Chen, T., Zhang, P., Zhang, H., Zheng, W., Ren, Z., et al. (2013). Illuminating the active Haiyuan fault, China by airborne light detection and ranging. *Chinese Science Bulletin*, *58*(1), 41–45.

Liu-Zeng, J., Klinger, Y., Xu, X., Lasserre, C., Chen, G., Chen, W., et al. (2007). Millenial recurrence of large earthquakes on the Haiyuan fault near Songshan, Gansu province, China. *Bulletin of the Seismological Society of America*, *97*(1B), 14–34. https://doi.org/10.1785/0120050118

Liu-Zeng, J., Shao, Y., Klinger, Y., Xie, K., Yuan, D., & Lei, Z. (2015). Variability in magnitude of paleoearthquakes revealed by trenching and historical records, along the Haiyuan Fault, China. *Journal of Geophysical Research: Solid Earth*, *120*, 8304–8333. https://doi.org/10.1002/2015JB012163

Marrero, S. M., Phillips, F. M., Borchers, B., Lifton, N., Aumer, R., & Balco, G. (2016). Cosmogenic nuclide systematics and the CRONUScalc program. *Quaternary Geochronology*, *31*, 160–187. https://doi.org/10.1016/j.quageo.2015.09.005

Meade, B. J., Klinger, Y., & Hetland, E. A. (2013). Inference of multiple earthquake-cycle relaxation timescales from irregular geodetic sampling of interseismic deformation. *Bulletin of the Seismological Society of America*, *103*(5), 2824–2835.

Meriaux, A. S., Ryerson, F. J., Tapponnier, P., Van der Woerd, J., Finkel, R. C., Xu, X. W., et al. (2004). Rapid slip along the central Altyn Tagh Fault: Morphochronologic evidence from Cherchen He and Sulamu Tagh. *Journal of Geophysical Research*, *109*, B06401. https://doi.org/10.1029/2003JB002558

Meriaux, A. S., Tapponnier, P., Ryerson, F. J., Xu, X., King, G. C. P., Van der Woerd, J., et al. (2005). The Aksay segment of the northern Altyn Tagh fault: Tectonic geomorphology, landscape evolution, and Holocene slip-rate. *Journal of Geophysical Research*, *110*, B04404. https://doi.org/10.1029/2004JB003210

Meriaux, A. S., Van Der Woerd, J., Tapponnier, P., Ryerson, F., Finkel, C. F., Lasserre, C., & Xu, X. (2012). The Pingding segment of the Altyn Tagh Fault (91°E): Holocene slip-rate determination from cosmogenic dating of offset fluvial terraces. *Journal of Geophysical Research*, *117*, B09406. https://doi.org/10.1029/2012JB009289

Meyer, B., Tapponnier, P., Bourjot, L., Metivier, F., Gaudemer, Y., Peltzer, G., et al. (1998). Crustal thickening in Gansu-Qinghai, litospherique mantle subduction, and oblique, strike-slip controlled growth of the Tibet plateau. *Geophysical Journal International*, *135*, 1–47.

Min, W., Zhang, P. Z., & Deng, Q. D. (2001). The study of Holocene Paleoearthquakes on Zhongwei Tongxin fault zone. *Seismology and Geology*, *23*(3), 357–366.

Pan, G., Ding, J., Yao, D., & Wang, L. (2004). *Guidebook of 1:1,500,000 geologic map of the Qinghai-Xizang (Tibet) plateau and adjacent areas* (p. 48). Chengdu: China, Chengdu Publishing House.

Peltzer, G., & Saucier, F. (1996). Present-day kinematics ofAsia derived from geologic fault rates. *Journal of Geophysical Research*, *101*(B12), 27,943–27,956.

Peltzer, G., & Tapponnier, P. (1988). Formation and evolution of strike-slip faults, rifts, and basins during the India-Asia collision: An experimental approach. *Journal of Geophysical Research*, *93*(B12), 15,085–15,117.

Peltzer, G., Tapponnier, P., Gaudemer, Y., Meyer, B., Guo, S., Yin, K., et al. (1988). Offset of late Quaternary morphology, rate of slip, and reccurence of large earthquakes on the Chang Ma fault (Gansu, China). *Journal of Geophysical Research*, *93*(B7), 7793–7812. https://doi.org/10.1029/JB093iB07p07793

Peltzer, G., Tapponnier, P., Zhang, Z., & Xu, Z. Q. (1985). Neogene and Quaternary faulting in and along the Qinling Shan. *Nature*, *317*, 500–505. https://doi.org/10.1038/317500a0

Perrineau, A., Van der Woerd, J., Gaudemer, Y., Liu-Zeng, J., Pik, R., Tapponnier, P., et al. (2011). Incidion of the Yellow River in the Northeastern Tibet constrained by 10Be and 36Al cosmogenic isotop dating of fluvial terraces: Implication for catchment evolution and plateau building. *Geological Society of London, Special Publication*, *353*, 189–219. https://doi.org/10.1144/SP353.10

Poisson, B., & Avouac, J.-P. (2004). Holocene hydrological changes inferred from alluvial stream entrenchment in north Tian Shan (northwestern China). *The Journal of Geology*, *112*(2), 231–249.

Ren, Z., Zhang, Z., Chen, T., Yan, S., Yin, J., Zhang, P., et al. (2016). Clustering of offsets on the Haiyuan fault and their relationship to paleoearthquakes. *Geological Society of America Bulletin*, *128*(1-2), 3–18.

Repka, J. L., Anderson, R., & Finkel, R. (1997). Cosmogenic dating of fluvial terraces, Fremont River, Utah. *Earth and Planetary Science Letters*, *152*, 59–73.

Rosenthal, Y., Linsley, B. K., & Oppo, D. W. (2013). Pacific Ocean heat content during the past 10,000 years. *Science*, *342*(6158), 617–621. https://doi.org/10.1126/science.1240837

Rosu, A.-M., Pierrot-Deseilligny, M., Delorme, A., Binet, R., & Klinger, Y. (2015). Measurement of ground displacement from optical satellite image correlation using the free open-source software MicMac. *ISPRS Journal of Photogrammetry and Remote Sensing*, *100*, 48–59.

Ryerson, F., Tapponnier, P., Finkel, R., Mériaux, A., Van der Woerd, J., Lasserre, C., et al. (2006). Application of cosmogenic nuclides to the study of Earth surface processes: The practice and the potential. *Geological Society of America Special Papers*, *415*.

Saint-Carlier, D., Charreau, J., Lavé, J., Blard, P.-H., Dominguez, S., Avouac, J.-P., & Wang, S. (2016). Major temporal variations in shortening rate absorbed along a large active fold of the southeastern Tianshan piedmont (China). *Earth and Planetary Science Letters*, *434*, 333–348. https://doi.org/10.1016/j.epsl.2015.11.041

Sieh, K., & Jahns, R. (1984). Holocene activity of the San Andreas fault at Wallace Creek, California. *GSA Bulletin*, *95*(8), 883–896.

Stone, J. O. (2000). Air pressure and cosmogenic isotope production. *Journal of Geophysical Research*, *105*(B10), 23,753–23,759.

Styron, R. (2015), Slip-rate calculator, edited, https://github.com/cossatot/slip_rate_calculator.

Su, Q., Ren, Z., Zhang, H., Zhang, P., & Manopkawee, P. (2019). The role of the Haiyuan fault in accelerating incision rate of the Yellow River at the Mijia Shan area, northeastern Tibetan plateau, as revealed by in-situ ^{10}Be. *Journal of Asian Earth Sciences*, *179*, 276–286.

Tapponnier, P., & Molnar, P. (1977). Active faulting and tectonics in China. *Journal of Geophysical Research*, *82*, 2905–2930.

Van der Woerd, J., Klinger, Y., Sieh, K., Tapponnier, P., Ryerson, F. J., & Meriaux, A. S. (2006). Long-term slip rate of the southern San Andreas Fault from Be-10-Al-26 surface exposure dating of an offset alluvial fan. *Journal of Geophysical Research*, *111*, B04407. https://doi.org/10.1029/2004JB003559

Van Der Woerd, J., Ryerson, F. J., Tapponnier, P., Gaudemer, Y., Finkel, R., Meriaux, A. S., et al. (1998). Holocene left slip-rate determined by cosmogenic surface dating on the Xidatan segment of the Kunlun fault (Qinghai, China). *Geology*, *26*, 695–698.

Van Der Woerd, J., Tapponnier, P., Ryerson, F. J., Meriaux, A. S., Meyer, B., Gaudemer, Y., et al. (2002). Uniform postglacial slip-rate along the central 600 km of the Kunlun Fault (Tibet), from Al-26, Be-10, and C-14 dating of riser offsets, and climatic origin of the regional morphology. *Geophysical Journal International*, *148*(3), 356–388.

Van der Woerd, J., Xu, X. W., Li, H. B., Tapponnier, P., Meyer, B., Ryerson, F. J., et al. (2001). Rapid active thrusting along the northwestern range front of the Tanghe Nan Shan (western Gansu, China). *Journal of Geophysical Research*, *106*(B12), 30,475–30,504.

Weldon, R., & Sieh, K. (1985). Holocene rate of slip and tentative reccurence interval for large earthquakes on the San Andreas fault, Cajon Pass, southern California. *GSA Bulletin*, *96*(6), 793–812.

Weldon, R. J. II (1986). The Late Cenozoic geology of Cajon Pass; implications for tectonics and sedimentation along the San Andreas Fault. Dissertation (Ph.D.), California Institute of Technology. http://resolver.caltech.edu/CaltechETD:etd-08302006-135307

Xu, X., Yeats, R. S., & Yu, G. (2010). Five short historical earthquakes surface ruptures near the Silk Road, Gansu province, China. *Bulletin of the Seismological Society of America*, *100*(2), 541–561. https://doi.org/10.1785/0120080282

Yang, H., Yang, X., Huang, X., Li, A., Huang, W., & Zhang, L. (2018). New constraints on slip rates of the Fodongmiao-Hongyazi fault in the Northern Qilian Shan, NE Tibet, from the ^{10}Be exposure dating of offset terraces. *Journal of Asian Earth Science*, *151*, 131–147. https://doi.org/10.1016/j.jseaes.2017.10.034

Yang, Y., Liu, C. Q., Van der Woerd, J., Xu, S., Cui, L. F., Zhao, Z. Q., et al. (2019). New constraints on the late Quaternary landscape evolution of the eastern Tibetan Plateau from cosmogenic 10Be and 26Al analysis. *Quaternary Science Reviews*, *220*, 244–262.

Yao, W., Liu-Zeng, J., Oskin, M. E., Wang, W., Li, Z., Prush, V., et al. (2019). Reevaluation of the Late Pleistocene slip rate of the Haiyuan fault near Songshan, Gansu province, China. *Journal of Geophysical Research: Solid Earth*, *124*, https://doi.org/10.1029/2018JB016907

Zhang, P., Molnar, P., Burchfiel, B. C., Royden, L., Zhang, W., Jiao, D., et al. (1988). Bounds on the Holocene slip rate along the Haiyuan fault, north-central China. *Quaternary Research*, *30*, 151–164.

Zhang, W., Jiao, D., Zhang, P., Molnar, P., Burchfiel, B. C., Deng, Q., et al. (1987). Displacement along the Haiyuan fault associated with the great 1920 Haiyuan, China, earthquake. *Bulletin of the Seismological Society of America*, *77*, 117–131.

Zheng, W. J., Zhang, P. Z., He, W. G., Yuan, D. Y., Shao, Y., Zheng, D. W., et al. (2013). Transformation of displacement between strike-slip and crustal shortening in the northern margin of the Tibetan Plateau: Evidence from decadal GPS measurements and late Quaternary slip rates on faults. *Tectonophysics*, *584*, 267–280.